

POLITECNICO DI MILANO

Facoltà di Ingegneria Industriale e dell'Informazione

Corso di Laurea Magistrale in Ingegneria Spaziale

Dipartimento di Scienze e Tecnologie Aerospaziali



**Non-linear Spacecraft Component Parameters
Identification Based on Experimental Results and
Finite Element Model Updating**

Relatore: Prof. Sergio RICCI

Co-relatore: Ing. Marina BELLINI

**Tesi di Laurea di:
Serena Olga VISMARA
Matr. 799451**

Anno Accademico 2013-2014

A chi mi ha sopportata in questi anni

Abstract

This study aims at developing a procedure to identify and modelling the behaviour of structural elements that show a non-linear behaviour during tests. The structural element taken into account is part of the Intermediate eXperimental Vehicle, that successfully completed its 100-minute mission on 11 February 2015. The element under investigation is the flap developed under the responsibility of Thales Alenia Space Italia, the major contractor, which provided the experimental data needed to accomplish the investigation.

In this study the application of the Restoring Force Surface method (or equivalently, the Force State Mapping Technique) as a strategy to characterize and identify localized non-linearities has been investigated. This method, which works in the time-domain, has been chosen because it has 'built-in' characterization capabilities, it allows a direct non-parametric identification of non-linear systems (in so far as Single-Degree-of-Freedom systems are considered) and it can easily deal with sine-sweep excitations.

Firstly, the method implementation was validated by means of several numerical simulations. Then it was applied to a simple experimental case prepared on purpose: a clamped beam which showed a non-linear behaviour characterized by a piecewise linear stiffness. Having obtained satisfactory results in the previous steps, the identification of the non-linearity present in a real structure, the IXV flap, was attempted.

Once the non-linear parameters were identified, they were used to update the finite element model in order to prove its capability of predicting the flap behaviour for different load levels.

The novelty of this work lies in the application of the method to experimental data coming from tests which, in addition, were not meant for this purpose.

Keywords: Non-linear system identification, Restoring force surface method, Finite element model updating

Sommario

Questo lavoro di tesi nasce con lo scopo di mettere a punto una procedura che permetta di identificare e modellare il comportamento di componenti strutturali che mostrano un comportamento non-lineare durante i test. L'elemento strutturale preso in considerazione fa parte del dimostratore IXV (Intermediate eXperimental Vehicle), che ha completato con successo la missione il giorno 11 Febbraio 2015. L'elemento di studio è rappresentato dal flap sviluppato sotto la responsabilità di Thales Alenia Space Italia, prime contractor, la quale ha fornito i dati sperimentali che hanno permesso di completare l'analisi.

La tesi esamina l'applicazione del Restoring Force Surface method (o dell'equivalente Force State Mapping Technique) come strategia per caratterizzare e identificare non-linearità localizzate. Questo metodo, definito nel dominio del tempo, è stato scelto per la sua intrinseca capacità di caratterizzazione, perchè permette l'identificazione non-parametrica di sistemi non-lineari (limitandosi a sistemi ad un solo grado di libertà) e perchè permette di gestire facilmente eccitazioni di tipo sine-sweep.

Inizialmente, l'implementazione del metodo è stata convalidata attraverso diverse simulazioni numeriche. Successivamente, esso è stato applicato ad un semplice caso sperimentale preparato appositamente: una trave incastrata caratterizzata da una curva di rigidità lineare a tratti. Avendo ottenuto risultati soddisfacenti nei passaggi precedenti, è stata tentata l'identificazione della non-linearità presente in una struttura reale: il flap del modulo IXV sviluppato da Thales Alenia Space.

Una volta che i parametri della non-linearità sono stati identificati, essi vengono usati per aggiornare il modello ad elementi finiti in modo da verificarne la capacità di predire il comportamento del flap per diversi livelli di carico.

La novità di questo lavoro risiede nell'applicazione del metodo a dati sperimentali ottenuti da test che inoltre non erano intesi per questo scopo.

Parole chiave: Identificazione di sistemi non-lineari, Restoring force surface method, Aggiornamento modello ad elementi finiti

Acknowledgements

I am most grateful to my supervisor, Prof. Sergio Ricci, for his sustained encouragement, interest and guidance given over the period in which the research work herein presented has been carried out.

I am indebted to Thales Alenia Space (Turin facility) and its managers and employees for serving as host and advisers to me for all these months as I performed the core of my research. In particular, I would like to thank Marina Bellini, who graciously tutored me. I would also like to thank Laura Trittoni and Stefano Destefanis, who provided feedback and guidance along the way. For the friendly cooperation and useful discussions throughout the period of research, I wish to express my gratitude to Roberto Ullio, Jurij D'amico, Dario Luison, Francesco Quagliotti, Luca Tizzani, Marco Notarnicola, Giovanni Murgia and Pietro Nali.

Thanks are also due to Dr. Mauro Terraneo for his valuable help during the experimental work at the laboratory.

I am grateful to Prof. Keith Worden (University of Sheffield) for answering my questions and for his book, which introduced me to the topic of non-linear dynamics.

Many thanks to my colleagues and friends for their support during all these years. I would like to mention Lucia Principito, Claudio Tagliabue, Stefano Losa and Alessandro Gilardelli.

Finally, words would never be enough to thank my family (grandparents included), Gionata and Annalisa for their un-conditional encouragement and support through thick and thin of my studies.

Contents

1	Introduction	1
1.1	Background of the problem	1
1.2	Non-linear system identification	2
1.2.1	Non-linearity detection	3
1.2.2	Non-linearity characterization	4
1.2.3	Non-linear parameters extraction	5
1.3	The Restoring Force Surface method	5
1.4	Objectives of the thesis	6
1.5	Organization of the thesis	7
2	The Restoring Force Surface Method	9
2.1	Theoretical background	9
2.1.1	Sections	10
2.1.2	Base excitation	11
2.2	Data processing	12
2.2.1	Time-domain integration	12
2.2.2	Filtering	13
3	Numerical Simulations	19
3.1	Excitation signals	19
3.1.1	Steady-state sine excitation	20
3.1.2	Sine-sweep excitation	20
3.2	ODE solver	21
3.3	Linear system	22
3.4	Bilinear stiffness	24

3.5	Non-linear damping	27
4	FE modelling of gap	29
4.1	Linear plate analysis	29
4.2	Gap modelling and non-linear parameters identification	32
4.3	Sine-sweep excitation	35
4.3.1	Comparison with SOL400	37
4.4	Non-linear harmonic response	39
4.5	Enforced acceleration	44
5	Experimental study of a beam	49
5.1	Low excitation test	50
5.2	High excitation test	53
5.3	Velocity estimation via Kalman filter	55
6	Application to the IXV flap	61
6.1	The Intermediate eXperimental Vehicle	62
6.1.1	Mission overview	62
6.1.2	The vehicle	63
6.2	Experimental results	64
6.3	Non-linearity parameters identification	68
6.4	FE model update	70
6.4.1	Non-linear transient analysis	70
7	Conclusions and Future Work	75
A	Harmonic Balance Method	77
B	Nastran input files	83
C	Macaulay's method for beam deflection	87
D	Kalman filter MATLAB code	91
	Bibliography	95

List of Figures

1.1	Non-linear system identification process [1]	3
1.2	Real and imaginary part of FRF for different excitation force levels	4
1.3	Idealized forms of common types of structural non-linearities . . .	5
1.4	Thesis organization	8
2.1	Schematic of the based-excited system [13]	11
2.2	Non-linear phase filter	14
2.3	Bidirectional recursive filter [20]	15
2.4	Block diagram of the bidirectional filtering (* means convolution)	16
2.5	Effect of zero-phase and linear phase filters on signals	16
2.6	Poles and zeros of a 4 th order stable filter	17
2.7	Gain comparison of a high-pass filters	18
3.1	Comparison between stiff and non-stiff ODE solvers [28]	22
3.2	Sine sweep excitation for linear and bilinear stiffness systems . . .	23
3.3	Restoring force surface - linear system	23
3.4	Exact and estimated stiffness curves - linear system	24
3.5	Restoring force surfaces - bilinear system	26
3.6	Exact and estimated stiffness curves - bilinear system	26
3.7	Restoring force surface - non-linear damping system	28
3.8	Exact and estimated damping curves - non-linear damping system	28
4.1	Plate FE model	30
4.2	Plate dynamic responses	30
4.3	RFS - linear plate (node 353 fully constrained)	31

4.4	RFS - linear plate (node 353 free in the z direction)	31
4.5	Time response at node 353 when the z dof is left free	33
4.6	Restoring force surface symmetric gap	34
4.7	Acceleration at node 176 (\simeq CoG) - input given as LOAD	36
4.8	Restoring force surface - sine-sweep excitation	36
4.9	Acceleration (SOL400)	37
4.10	Velocities comparison	38
4.11	Displacements comparison	38
4.12	Polynomial approximation of the gap	40
4.13	Response comparison for load level 1: 0.1 N	41
4.14	Linear frequency response for unconstrained z dof at node 353	42
4.15	Response comparison for load level 2: 1 N	42
4.16	Response comparison for load level 3: 10 N	42
4.17	Response comparison for load level 4: 100 N	43
4.18	Frequency response when the z dof at node 353 is constrained	43
4.19	Plate homogeneity test	43
4.20	Accelerations comparison - DEM and LMM	45
4.21	Effect of the rigid-body drift on the displacement	46
4.22	Relative acceleration obtained running the LMM in SOL129	47
5.1	Beam test set-up	50
5.2	Force time history - linear test	52
5.3	Measured responses - linear test	52
5.4	Restoring Force Surface method applied to the linear beam	53
5.5	Homogeneity test for the cantilever beam	53
5.6	Force time history - high excitation test	54
5.7	Measured responses - high excitation test	54
5.8	Restoring Force Surface method applied to the non-linear beam	55
5.9	The discrete Kalman filter loop	57
5.10	Comparison between integrated and estimated velocity	59
5.11	Magnification of Fig.(5.10)	59
6.1	IXV mission profile	63
6.2	IXV external layout	64

6.3	Flap Control System	64
6.4	Flap testing set-up	65
6.5	Input excitations IXV test	65
6.6	Frequency responses from test	66
6.7	Homogeneity test - IXV flap	66
6.8	Acceleration measured at the tip	67
6.9	Acceleration measured at the centre of mass	67
6.10	Input acceleration time histories	68
6.11	RFS method applied to the data from the first test	69
6.12	RFS method applied to the data from the second test	69
6.13	Acceleration responses at CoG for excitation level 1	70
6.14	Acceleration at the enforced node	71
6.15	Linear SOL129 (without the gap element)	71
6.16	Flap FE model	72
6.17	Time response obtained for $W3 = 194.78 \text{ rad/s}$	73
6.18	Acceleration responses at CoG in the presence of the gap	73
6.19	Frequency responses calculated from transient responses	74
C.1	Scheme of cantilever beam to apply the Macaulay's method	87

List of Tables

3.1	Identification results for the linear case	24
3.2	Identification results for the bilinear case	25
3.3	Identification results for the non-linear damping case	27
4.1	Stiffness parameters benchmarks	31
4.2	Symmetric gap identified parameters	33
4.3	Symmetric gap identified parameters under sine-sweep excitation .	36
5.1	Dimensions and material constants for cantilever beam	50
5.2	Identified parameters for non-linear beam	54
6.1	Identified clearance values	69

Chapter 1

Introduction

This chapter presents a brief introduction to the subject of non-linear structural dynamics. In the last section, the structure of the thesis and the relationship between different chapters are presented in order to give an overview of the thesis.

1.1 Background of the problem

Linear system identification is a discipline that has evolved considerably during the last 30 years. Modal analysis is the most popular approach to perform linear system identification in structural dynamics and its popularity stems from its great generality: modal parameters (natural frequencies, mode shapes and damping ratios) describe the behaviour of a system for any input type and any range of the input.

In the presence of non-linearity the basic principles that apply to a linear system and that form the basis of modal analysis are no longer valid. Therefore, it is necessary to apply a different strategy to detect, characterize and identify localized non-linearities.

Almost all practical structures are non-linear to some extent, the non-linearity being caused by one or a combination of factors. In structural dynamics, the most common types of non-linearities are [1]:

- Geometric non-linearity, which results when a structure undergoes large

displacements.

- Inertia non-linearity, which derives from non-linear terms containing velocities and/or accelerations in the equations of motion.
- Non-linear material behaviour, that can be observed when the constitutive law relating stresses and strains is non-linear.
- Damping dissipation: the modal damping assumption is not necessarily the most appropriate representation of the physical reality. Dry friction effects (bodies in contact, sliding with respect to each other) and hysteretic damping are examples of non-linear damping.
- Non-linearity in the boundary conditions (for example, vibro-impacts due to loose joints and clearances which possesses non-smooth force-deflection characteristics).

To predict the behaviour of non-linear systems, it is necessary to include the corresponding non-linear elements into the numerical/mathematical models which describe those systems. The parameters of such non-linear elements are case specific and there is no general analysis method for the development of structural models from experimental measurements, i.e. non-linear system identification, that can be applied to all systems in all instances.

1.2 Non-linear system identification

Non-linear system identification is part of the model validation process and it can be viewed as a succession of three steps (Fig.1.1): detection, characterization and parameter estimation. Once non-linear behaviour is detected, a non-linear system is said to be characterized after the location, type and functional form of the non-linearities are determined. The parameters of the selected model are then estimated using linear least-squares fitting or non-linear optimization algorithms.

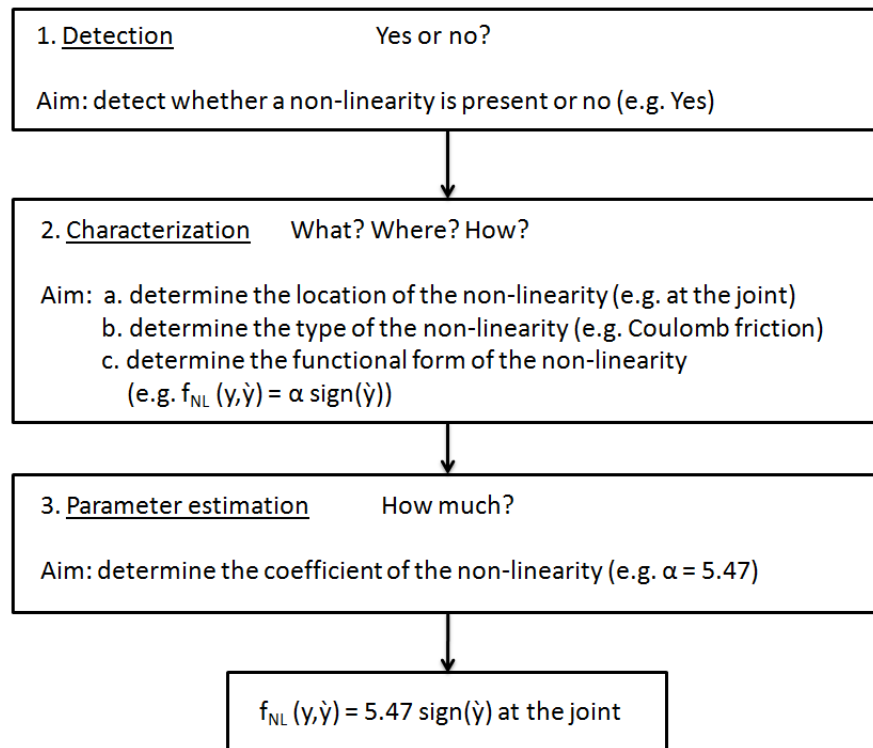


Figure 1.1: Non-linear system identification process [1]

1.2.1 Non-linearity detection

The detection of structural non-linearity is the first step toward establishing a structural model with a good predictive accuracy. A survey of the numerous non-linear system detection techniques for single-input-single-output systems can be found in [2] and [3].

The breakdown of the principle of superposition is a possible means of detecting the presence of a non-linear effect [4]. The test for homogeneity, which is a restricted form of the principle of superposition, is one of the most popular detection techniques. Homogeneity violation is best visualized in the frequency domain through comparison of frequency response functions (FRFs) for different excitation levels: if the FRFs for different levels overlay, linearity is assumed to hold. However, this method is not infallible as there are some systems (as discussed in Section 3.4) which are non-linear which nonetheless show homogeneity. The reason for this is that homogeneity is a weaker condition than

superposition.

An example of the application of the homogeneity test is shown in Fig.(1.2). The hardening behaviour of the non-linearity is translated into the shifting of the resonance frequency towards higher frequencies. An example of the homogeneity test applied to a real structure can be found in [5].

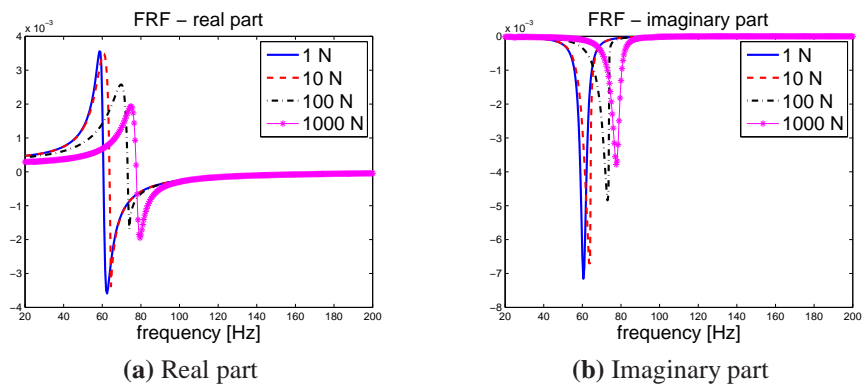


Figure 1.2: Real and imaginary part of FRF for different excitation force levels

1.2.2 Non-linearity characterization

A non-linear system is said to be characterised when the location, type and functional form of all the non-linearities throughout the system are determined.

The reason why the Restoring Force Surface method was chosen for this thesis is that it has 'built-in' characterization capabilities since it allows the three-dimensional visualization of the restoring force as a function of displacement and velocity. Moreover, a characterization of the elastic and dissipative forces can be obtained by taking a cross-section of this three-dimensional plot along the axes where either the velocity or the displacement is equal to zero, respectively. The resulting plots are termed stiffness and damping curves, respectively (examples of these curves are shown in Fig.(1.3)). and they represent a quick way for understanding what type of non-linearity is involved.

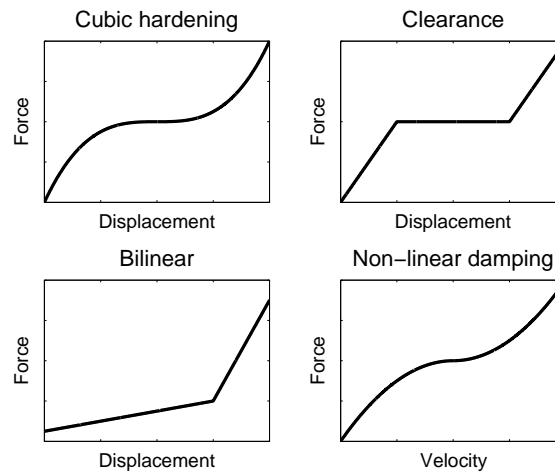


Figure 1.3: Idealized forms of common types of structural non-linearities

1.2.3 Non-linear parameters extraction

Parameter estimation is the last step. An important assumption which conditions the success of parameter estimation is that all the non-linearities have been properly characterised. A survey on the available methods to accomplish this step can be found in [1], [4] and [6].

In this thesis, the parameters will be extracted by curve-fitting the numerical/experimental data. Each time, the function to be fitted to the data will be chosen according to the type of non-linearity involved.

1.3 The Restoring Force Surface method

The Restoring Force Surface Method began with Masri and Caughey's paper in which they proposed a method to identify non-linear mechanical systems resulting in a modelling of the non-linear force as a function of the displacement and velocity. A parallel approach, named Force-State Mapping Technique, was developed independently by Crawley and Aubert and an application can be found in [7].

The method was first developed for SDOF systems, but the generalisation to lumped parameter MDOF systems soon followed. However, a further signal

processing demand arises, in fact displacement, velocity and acceleration data were required for each DOF necessitating the use of complex instrumentation or further numerical analysis. Some of these exceptions were overcome by Worden and Tomlinson [4].

Significant improvements were brought about since the original papers. Duym [8] applied the method to a damper showing that a more appropriate choice would be the use velocity and acceleration as independent variables. Duym and Schoukens [9] designed optimized excitation signals in order to guarantee the quality of the fit by uniformly covering the phase-plane. They also used a local non-parametric identification of the non-linear force [10]. Jalali *et al.* [11] showed that the complex phenomenon of energy dissipation in lap joints can be represented by a simple analytical model capable of producing accurate results. Shin and Hammond [12] suggested an alternative method which may be used when all the state variables are not available and when exact values of the system parameters do not need to be estimated.

Experimental investigations are performed in [13] [14] and [15]. In [16] a comparison between different techniques, namely the Restoring Force Surface Method, wavelet transform and Conditioned Reverse Path Method, is carried out using numerical data related to a real-world structure.

1.4 Objectives of the thesis

The objective of this thesis is the development of a procedure for structural non-linearity identification and FE model updating. The non-linearity parameters identification is carried out by means of the Restoring Force Surface method and the identified parameters are used to update the FE model. Different ways to update the model introducing non-linear elements will be analysed and compared both in the time and frequency domain.

1.5 Organization of the thesis

In this thesis, each chapter deals with a more complex system with respect to the one studied in the previous one, thus allowing to check the performance of the implemented method starting from simple numerical systems and moving on, step-by-step, towards more realistic systems (Fig. 1.4).

In fact, the method is first applied to simple numerical examples and, having obtained satisfactory results at this stage, it is tested on a more complex structure represented by a FE model of a plate. Finally, it has been applied to the data obtained from an experimental case prepared on purpose.

Since all these steps have produced satisfactory results, the implementation of the method has been proved to be reliable and can therefore be used to identify the non-linearity present in a real structure.

In details the topic of each chapter:

Chapter 2. The Restoring Force Surface Method This chapter presents the theory behind the chosen non-linear system identification method, which will be applied throughout the thesis. The data processing associated with the method is also presented.

Chapter 3. Numerical simulations The method implementation is tested by means of some simple numerical examples, simulated in MATLAB, which takes into account different types of non-linearities.

Chapter 4. FE modelling of a gap non-linearity A more realistic structure, represented by a plate, has been taken into account to further validate the method implementation. Moreover, different methods for modelling a clearance non-linearity in Nastran have been analysed in order to set the stage for the last step (Chapter 6).

Chapter 5. Experimental study of a piecewise linear beam As an intermediate step between the numerical simulations and the real-world structures, the method is applied to experimental data obtained testing a cantilever beam characterized by a piecewise linear stiffness. A procedure for estimating the missing velocity measurement from the acceleration and the displacement measurements by means of the Kalman filter has been presented.

Chapter 6. Application to a real-life structure: the IXV flap The method is used to characterize and to extract the parameters of the non-linearity which influenced the behaviour of the IXV flap during the tests. Once the non-linearity has been fully identified, the parameters are used to update the FE model in order to prove its capability of reproducing the flap behaviour.

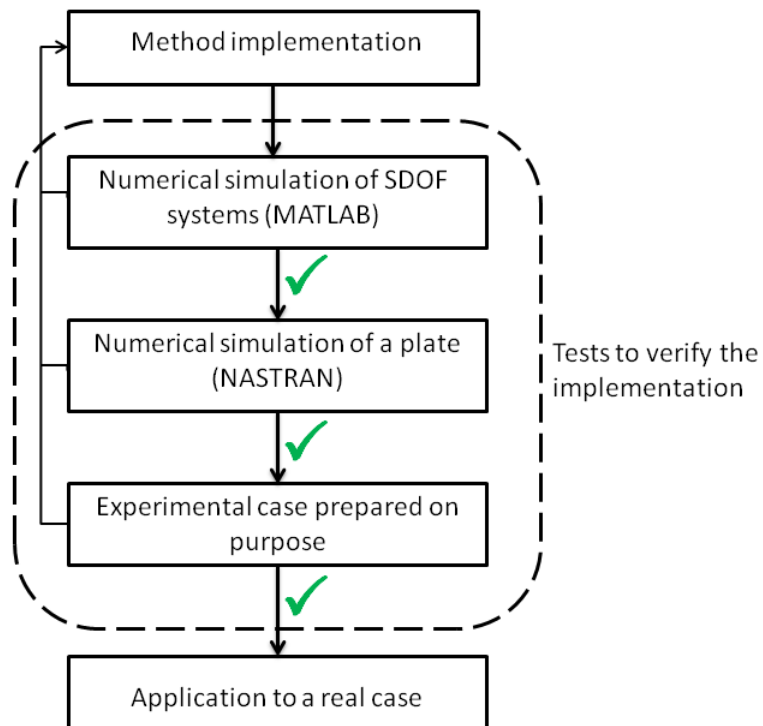


Figure 1.4: Thesis organization

Chapter 2

The Restoring Force Surface Method

2.1 Theoretical background

The procedure described in this section can be found in [4] and it is here reported for the sake of clarity. This method allows a direct non-parametric identification for SDOF non-linear systems and the only a priori information required is an estimate of the system mass.

The starting point is the equation of motion as specified by Newton's second law

$$m\ddot{y} + f(y, \dot{y}) = p(t) \quad (2.1)$$

where m is the mass (or an effective mass) of the system and $f(y, \dot{y})$ is the internal restoring force which acts to return the system to equilibrium when disturbed. The function f can be a general function of position $y(t)$ and velocity $\dot{y}(t)$. In the special case when the system is linear

$$f(y, \dot{y}) = c\dot{y} + ky \quad (2.2)$$

where c and k are the damping and stiffness constant respectively. Since f is assumed to be dependent only on y and \dot{y} , it can be represented by a surface over

the phase plane, i.e. the (y, \dot{y}) -plane. A rearrangement of equation (2.1) gives

$$f(y(t), \dot{y}(t)) = p(t) - m\ddot{y}(t) \quad (2.3)$$

If the mass m is known and the excitation $p(t)$ and acceleration $\ddot{y}(t)$ are measured, all quantities on the right-hand side of this equation are known and hence so is f . Measurements of a time signal entails sampling it at regularly spaced interval Δt . If $t_i = (i - 1)\Delta t$ denotes the i -th sampling instant, then at t_i equation (2.3) gives

$$f_i = f(y_i, \dot{y}_i) = p_i - m\ddot{y}_i \quad (2.4)$$

where $p_i = p(t_i)$ and $\ddot{y}_i = \ddot{y}(t_i)$ and hence f_i are known at each sampling instant. If the velocities \dot{y}_i and displacements y_i are also known (i.e. from direct measurement or from numerical integration of the sampled acceleration data), at each instant $i = 1, \dots, N$ a triplet (y_i, \dot{y}_i, f_i) is specified. The first two values indicate a point in the phase-plane, the third gives the height of the restoring force surface above that point.

To identify non-linear joint properties, the force transmitted by the joint has to be represented as a function of its mechanical state coordinates (x and \dot{x} across the joint). This implies that the joint needs to be separated from the whole structure, which is something usually not easy to perform.

In the next chapters the method will be tested on some numerical examples to verify its ability of correctly estimating the parameters related to the non-linearity.

2.1.1 Sections

The surface plot is a very useful tool to visualize the non-linearity acting in the system, but it is better to rely on a two-dimensional representation of the data for the parameters extraction.

The stiffness curve or section is obtained by choosing a narrow band of width δ , through the origin, parallel to the y -axis. All the pairs of values $(y_i, f(y_i, \dot{y}_i))$ with velocities such that $|\dot{y}_i| < \delta$ are recorded. The y_i values are saved and placed in increasing order. This gives a $y \rightarrow f$ graph which is a slice through the force surface at $\dot{y} = 0$. The same procedure can be used to obtain the damping curve at

$y = 0$. If the restoring force separates, i.e.

$$f(y, \dot{y}) = f_d(\dot{y}) + f_s(y) \quad (2.5)$$

the identification (i.e. curve fitting to) of the stiffness and damping sections is sufficient to identify the whole system.

2.1.2 Base excitation

The qualification of the structural design and the verification of the structural integrity of spacecrafts are usually carried out by means of base-shake sine tests. To analyse this configuration the beam in Fig.(2.1) has been considered.

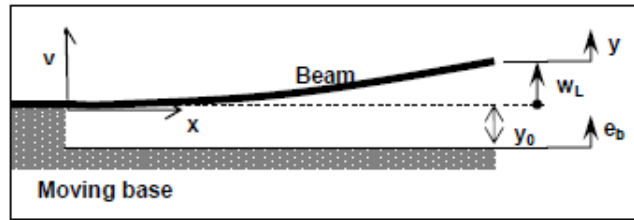


Figure 2.1: Schematic of the based-excited system [13]

The beam is excited around its first resonance, therefore it can be approximated as an oscillator subjected to base excitation. The oscillator is assumed to be connected to its base by a non-linear element. The base is allowed to move with acceleration $\ddot{e}_b(t)$ and this motion is transmitted to the mass through the non-linear spring and excites the response $\ddot{y}(t)$ of the mass. The equation of motion is

$$m\ddot{y} + f(w_L, \dot{w}_L) = 0 \quad (2.6)$$

where y is the absolute displacement of the beam tip and $w_L = y - e_b$ is the displacement of the beam tip relative to the substrate. In this configuration, the relative acceleration \ddot{w}_L would be computed and integrated to give \dot{w}_L and w_L . The advantage is that the mass only appears as a scaling factor and even if m is set to 1, the type of non-linearity can be represented faithfully. If an estimate of the mass becomes available, the force surface can be given the correct scale and the data can be used to fit a model.

2.2 Data processing

From the foregoing developments, it appears that displacement, velocity and acceleration data are all needed simultaneously at each sampling instant. The easiest approach to the procedure will be measuring one signal and estimate the other two from it by means of numerical integration or differentiation. Another strategy could be the one proposed by Crawley and O'Donnell [7], who measure displacement and acceleration and then form the velocity using a Kalman filter (this method will be discussed in details in Chapter 5).

Since numerical differentiation leads to inaccurate estimation of the acceleration, as shown in [4], the following discussion will focus on numerical integration only. More details about the various method for achieving integration can be found in [4] [18] [19].

2.2.1 Time-domain integration

The practical solution is to measure the acceleration and numerically integrate it to find velocity and displacement.

There are two main problems associated with numerical integration: the introduction of spurious low-frequency components into the integrated signal and the introduction of high-frequency pollution. Among all the various methods, the trapezium rule only suffers from the introduction of low-frequency components and does not require the use of a low-pass filter. Furthermore, it is the simplest integration process and offers considerable saving of time. For these reasons, the trapezium rule, expressed by equation (2.7), is considered throughout the thesis.

$$v_i = v_{i-1} + \frac{\Delta t}{2}(u_i + u_{i-1}) \quad (2.7)$$

where $v(t)$ is the estimated integral with respect to time of $u(t)$. Each step of

integration introduces an unknown constant of integration, so that

$$\dot{y}(t) = \int dt \ddot{y}(t) + A \quad (2.8)$$

$$y(t) = \left(\int dt \right)^2 \ddot{y}(t) + At + B \quad (2.9)$$

In the frequency domain, the effect of A and B manifests itself as a spurious low-frequency component as they affect the d.c. component of \dot{y} and y .

Usually, the constant of integration is fixed by initial data $\dot{y}(0)$, but, when dealing with a stream of time-data, this information is not available. However, under certain conditions ($p(t)$ is a zero-mean sequence and the non-linear restoring force $f(y, \dot{y})$ is an odd function of its argument), it can be assumed that $\dot{y}(t)$ and $y(t)$ are zero-mean signals. This means that A and B can be set to the appropriate values by removing the mean level from \dot{y} and a linear drift component from $y(t)$.

To prove what has been said it is useful to take a look at the transfer function of the trapezium rule, which is

$$H(\omega) = \frac{FT(\text{estimated results})}{FT(\text{true results})} = \cos(\omega/2) \frac{\omega/2}{\sin(\omega/2)} \quad (2.10)$$

where FT is the Fourier transform and ω the normalized frequency (the frequency of interest divided by the sampling frequency). Equation (2.10) means that the trapezium rule only integrates constant signals without error and underestimates the integral at all other frequencies.

Since the trapezium rule acts as an amplifier of the low-frequency components, high-pass filtering becomes necessary.

2.2.2 Filtering

Filtering is a frequency selective process that attenuates certain bands of frequencies while passing others.

As mentioned earlier, the results of the double integration by means of the trapezium rule need to be high-pass filtered to be cleaned totally. Choosing a cut-

off frequency higher than 0 Hz imposes the filtered signals to be of zero-mean since a polynomial trend of order 0, i.e. a constant, is removed.

In order to zero the phase lags introduced by the filter, data must be passed through any filter in both forward and backward directions. In fact, the impulse response of a recursive filter¹ is not symmetrical between left and right, therefore IIR (Infinite Impulse Response) filters are characterised by having a non-linear phase, as shown in Fig.(2.2). Any phase lags will destroy the simultaneity of the signals and will have disastrous effects on the estimated force surface.

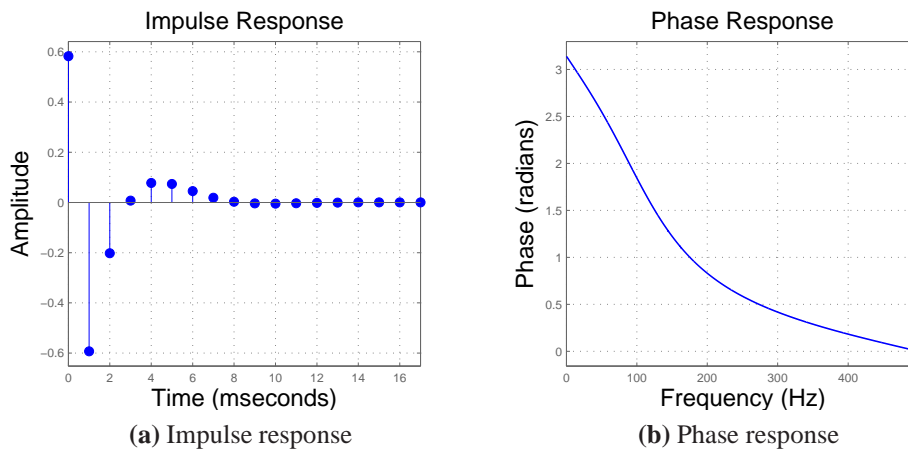


Figure 2.2: Non-linear phase filter: the impulse response is not symmetrical between the left and right and the phase is not a straight line

The penalty of this bidirectional filtering technique is a factor of two in execution time and program complexity. Moreover, it can be applied on stored data only (no real-time filtering), in fact when filtering forward and backward causality² is lost.

When filtering in both directions, the magnitude of the frequency response is the same for each direction, while the phases are opposite in sign. If the two directions are combined, the magnitude becomes squared (which means that the order of the filter is doubled), while the phase cancels to zero. Fig.(2.3) shows an example of how the bidirectional filtering works.

¹Recursive filters are described by the so called recursion equation: $y(n) = a_0x(n) + a_1x(n-1) + a_2x(n-2) + a_3x(n-3) + \dots + b_1y(n-1) + b_2y(n-2) + b_3y(n-3) + \dots$

²A system is causal if, for every choice of n_0 , the output sequence value at the index $n = n_0$ depends only on the input sequence values for $n \leq n_0$. This implies that if $x_1(n) = x_2(n)$ for $n \leq n_0$, then $y_1(n) = y_2(n)$ for $n \leq n_0$. The system is non-anticipative [21]

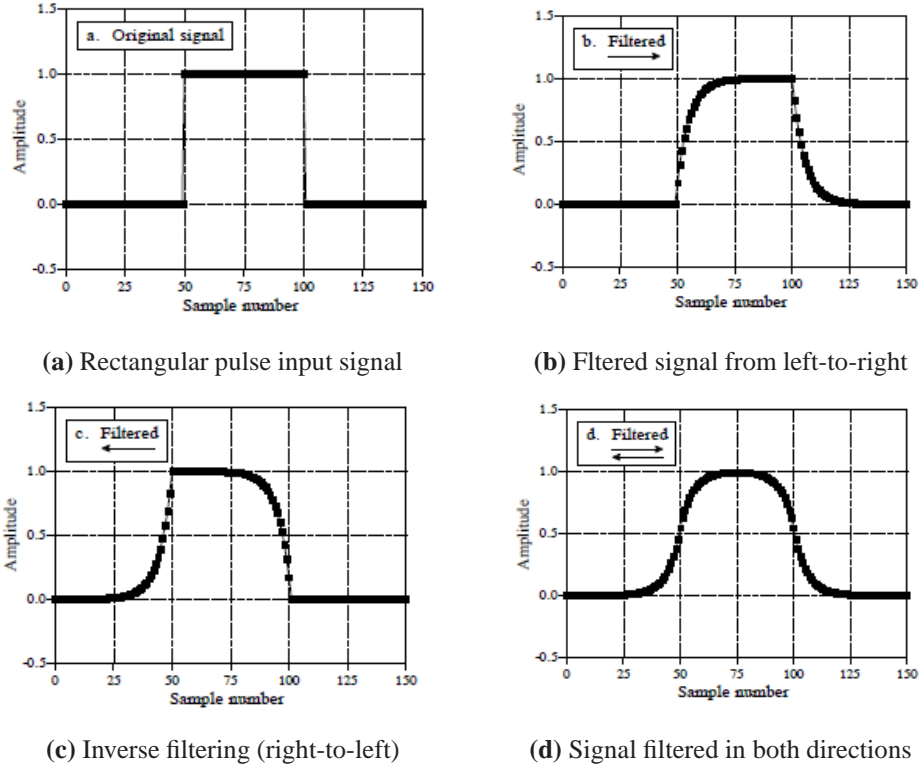


Figure 2.3: Bidirectional recursive filter [20]

This can be best seen in the frequency domain: if $x(n)$ is the input sequence and $h(n)$ is the filter's impulse response, the result of the first filter pass is

$$Z(e^{j\theta}) = X(e^{j\theta})H(e^{j\theta})$$

with $X(e^{j\theta})$ and $H(e^{j\theta})$ the Fourier transforms of $x(n)$ and $h(n)$, respectively. Time reversal corresponds to replacing θ by $-\theta$ in the frequency domain, therefore the result of the time reversal is

$$W(e^{j\theta}) = X(e^{-j\theta})H(e^{-j\theta})$$

The second filter pass corresponds to another multiplication by $H(e^{j\theta})$, yielding

$$V(e^{j\theta}) = H(e^{j\theta})W(e^{j\theta}) = |H(e^{j\theta})|^2 X(e^{-j\theta})$$

which after time-reversal gives the spectrum of the output signal

$$Y(e^{j\theta}) = |H(e^{j\theta})|^2 X(e^{j\theta}) \quad (2.11)$$

Equation(2.11) shows that the output spectrum is obtained by filtering with a filter with frequency response $|H(e^{j\theta})|^2$ which is real-valued, i.e. its phase is zero and consequently there are no phase distortions. The block diagram of the process is shown in Fig.(2.4). In MATLAB the function `filtfilt` [22] eliminates phase distortion using the information in the signal at points before and after the current point.

The comparison between a zero-phase filter and a linear phase filter is shown in Fig.(2.5).

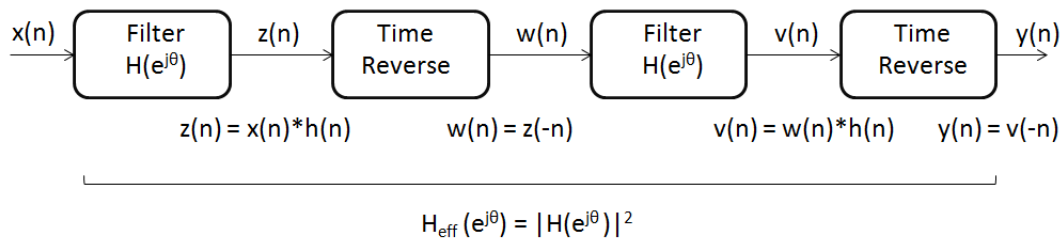


Figure 2.4: Block diagram of the bidirectional filtering (* means convolution)

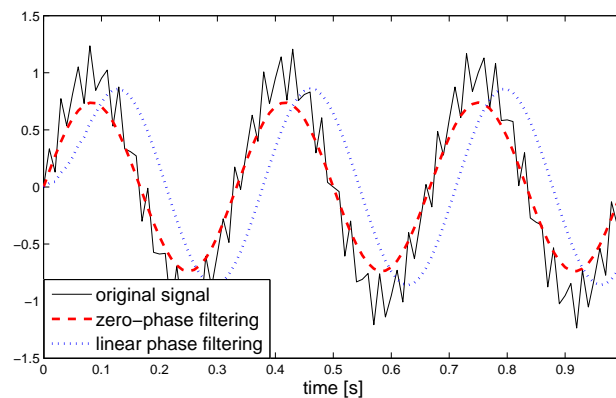


Figure 2.5: Effect of zero-phase and linear phase filters on signals

The last issue is related to stability. IIR filters may have both zeros and poles

on the z -plane³. As such, they are not guaranteed to be stable (an example of stable filter is shown in Fig. 2.6).

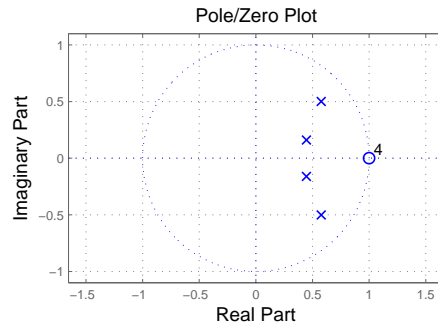


Figure 2.6: Poles and zeros of a 4th order stable filter

The IIR filters behaviour can be improved by means of cascaded structures: a high-performance filter is implemented as a combination of cascaded lower performance filters. This allows the computation of the roots of a lower order polynomial, thus reducing the round-off errors.

The resultant transfer function of two cascaded filter transfer functions is the product of those functions

$$H_{cas}(z) = H_1(z)H_2(z) \quad (2.12)$$

with an overall frequency response of

$$H_{cas}(\omega) = H_1(\omega)H_2(\omega) \quad (2.13)$$

and the resultant impulse response of cascaded filters is the convolution of their individual impulse responses. A more detailed discussion on filters stability and cascading IIR filters can be found in [21] and [23].

³In the z -plane the region of filter stability is mapped to the inside of the unit circle. If all poles are located inside the unit circle, the filter is stable

Butterworth filters

Butterworth filters are an example of IIR filters. They are defined by the property that the magnitude response is maximally flat in the passband and rolls off towards zero in the stopband. Moreover, the magnitude response is monotonic in the passband and in the stopband.

Compared with Chebyshev filters or elliptic filters, the Butterworth filters have a slower roll-off and thus will require a higher order to implement a particular stopband specification, but they have no ripple, as shown in Fig.(2.7).

Thanks to their ability to give a filtered signal with little to no losses, Butterworth filters have been used throughout this thesis. In MATLAB the function `butter` [22] allows the design of a n-th order digital Butterworth filter.

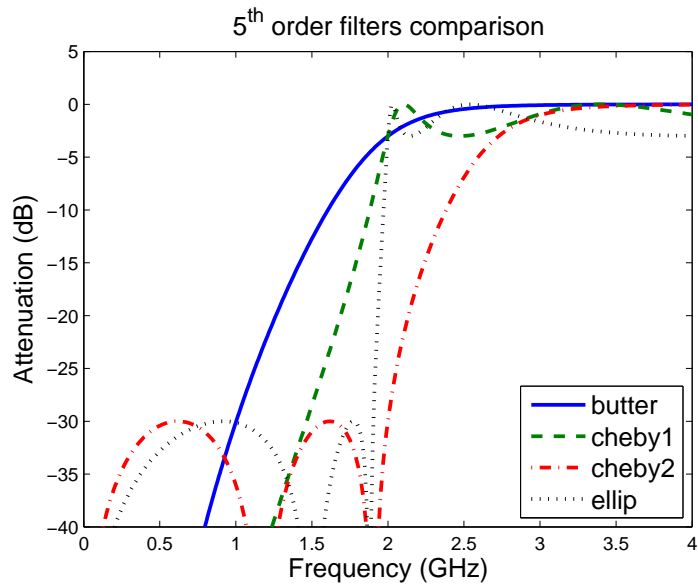


Figure 2.7: Gain comparison of a high-pass Butterworth filter and other common filter types

Chapter 3

Numerical Simulations

The Restoring Force Surface method described in the previous section is here applied on some numerical simulations in order to test it for different non-linearities. The method is first applied to a linear system and then tested on two different non-linear cases:

- an asymmetrical system characterized by a bilinear stiffness
- a symmetrical system characterized by non-linear damping

In the following, a brief discussion on the simulations setting is presented.

3.1 Excitation signals

In the Restoring Force Surface method the non-linear force is fitted to a series of standard functions. In order to guarantee the quality of the fit a sufficiently uniform distribution of the state trajectory sample points over the phase plane is needed.

A problem in the final step of the procedure is to perform a valid interpolation from randomly or irregularly spaced points in the plane to regular grid points. To improve the accuracy, a minimum number of points must be located in the neighbourhood of each grid point. The effects of different types of excitation on the non-linearities identification procedure are extensively discussed in [4] while

Duym [9] proposed a method to optimise the phase spectrum so that uniform coverage is obtained.

The excitation signals here considered for the numerical simulations are the steady-state sine excitation and the sine-sweep excitation.

3.1.1 Steady-state sine excitation

The use of sinusoidal excitation usually produces the most vivid effects from non-linear systems. Moreover, all the input energy is concentrated at the frequency of excitation and it is simple to eliminate noise and harmonics in the response signal.

As such, the signal-to-noise ration is very good and the result is a well-defined FRF with distortions arising from non-linearity being very clear, particularly when a constant magnitude force excitation is used.

3.1.2 Sine-sweep excitation

Sine-sweep excitation is a form of transient excitation and its effects on structural responses have been analysed in different papers: Gloth and Sinapius [24] showed that the maximum response for a resonance is lower than the maximum response expected for a harmonic excitation with the corresponding resonance frequency and there is a time delay for the maximum; Lollock [25] analysed the effect that sweep rates have on response amplitude and estimates of resonant frequency and damping for a SDOF system, whereas Nali and Bettacchioli [26] extended the analysis to MDOF systems and analysed the beating phenomena.

Sine-sweep excitation can be linear or exponential and can be expressed as

$$p(t) = A \sin(\phi(t)) \quad (3.1)$$

where A is the amplitude and $\phi(t)$ is the argument, phase, of the sine. The pulsation of the sweep is calculated as

$$\phi(t) = \int_0^t \Omega(\tau) d\tau \quad (3.2)$$

where $\Omega(\tau)$ indicates the instantaneous excitation frequency ¹. If an exponential sweep is considered

$$\Omega(\tau) = \Omega_0 2^{(R/60 \tau)} \quad (3.3)$$

where Ω_0 indicates the starting frequency of the sweep and the sweep-rate R is expressed in [*oct/min*].

After the integration, the phase is given by

$$\phi(t) = 2\pi \frac{60f_0}{R \ln(2)} (2^{(R/60 t)} - 1) + \phi_0 \quad (3.4)$$

3.2 ODE solver

MATLAB has a number of tools for numerically solving ordinary differential equations. The ODE suite has seven routines, which can be divided in two main categories, stiff ² and non-stiff, according to the kind of equations they can be applied to. Stiff solvers are implicit.

Stiffness is an efficiency issue: non-stiff methods can solve stiff problems, but they take a longer time. To better show the difference in the results obtained with stiff and non-stiff solvers, the results of the flame example in [28] are reported in Fig.(3.1), where it is evident that `ode23s` takes many fewer steps than `ode45`.

Since the equations to be solved for the following numerical simulations are all stiff, the stiff solvers will be preferred. The one used in the following simulation is the `ode15s`, which is a variable-order solver (the order can vary between 1 and 5) based on the Numerical Differentiation Formulas (NDF). NDFs are the default for `ode15s`, but it is possible to use another variant of linear multistep method, the Backward Differentiation Formulas (BDF). Since NDFs can take larger steps than BDFs maintaining the same accuracy, they have been chosen for the following simulations.

¹The instantaneous frequency defines the location of the signal's spectral peak as it varies with time. It may be interpreted as the frequency of a sine wave which locally fits the signal [27].

²An Initial Value Problem is stiff in some interval $[0 b]$ if the step size needed to maintain stability of the forward Euler method is much smaller than the step size required to represent the solution accurately. (U.M. Ascher, L.P. Petzold, *Computer methods for ordinary differential equations and differential-algebraic equations*)

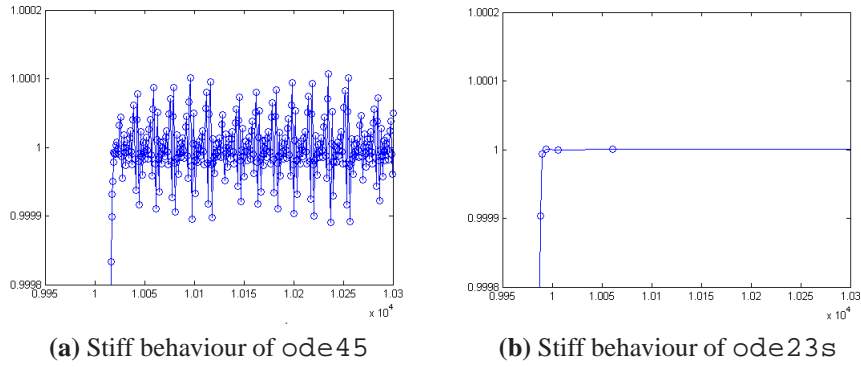


Figure 3.1: Comparison between stiff and non-stiff ODE solvers [28]

3.3 Linear system

For a linear system, the restoring force surface is a plane whose slope in the displacement direction represents the stiffness and the slope in the velocity direction represents the damping.

The simulation has been run considering equation (3.5)

$$25\ddot{x} + 15\dot{x} + 330000x = p(t) \quad (3.5)$$

where both the steady-state sine and the sweep-sine excitation have been considered as forcing functions $p(t)$.

For the steady-state sine excitation, $p(t)$ takes the following form:

$$p(t) = 100 \sin(\omega t)$$

where ω has been chosen equal to the first natural frequency of the system ($\simeq 115 \text{ rad/s}$). The simulation has been run for 10 s and the sampling frequency has been set to 1000 Hz.

In the case of the exponential sine-sweep, the excitation is given by

$$p(t) = A t \sin(\phi(t)) \quad (3.6)$$

where $A = 1$ and $\phi(t)$ takes the form explained in Section 3.1.2. The sweep-rate R is set to 4 oct/min and the frequency range is 5-120 Hz. In Fig.(3.2) the time

domain and time-frequency (spectrogram³) representations of the excitation are shown. This amplitude modulated signal will produce an increasing spiral shape in the phase-space, thus providing a fairly dense set of measurement points.

The results of the two simulations are shown in Fig.(3.3),(3.4) and collected in Table (3.1). The stiffness curves have been obtained by applying the procedure described in Section 2.1.1 and they are compared with the exact ones.

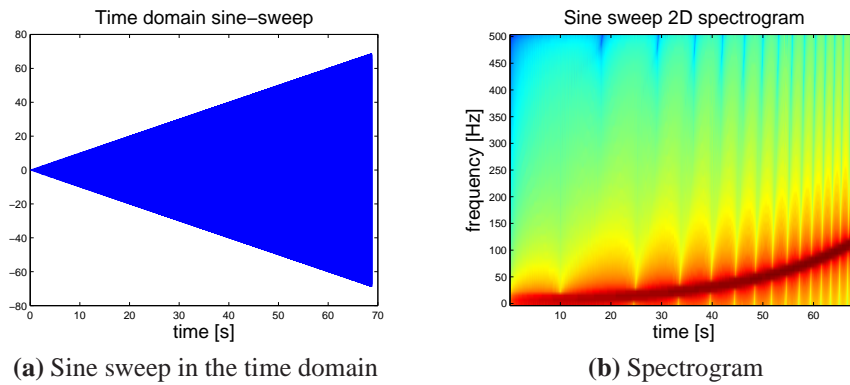


Figure 3.2: Sine sweep excitation for linear and bilinear stiffness systems

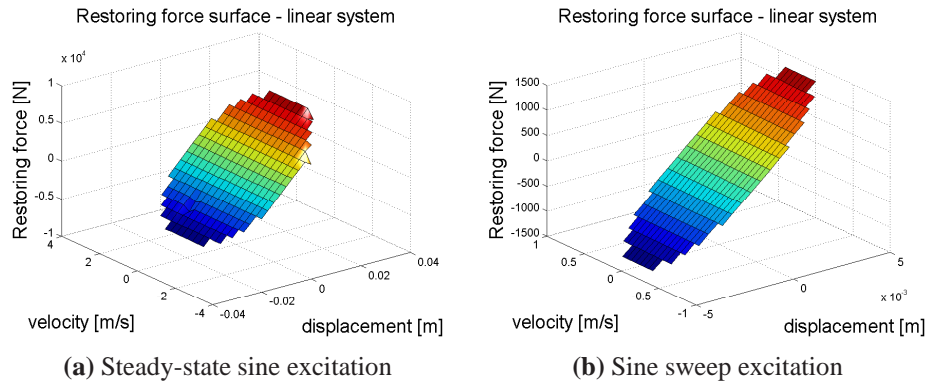


Figure 3.3: Restoring force surface - linear system

³The spectrogram is computed as $spectr(\tau, \omega) = |STFT(\tau, \omega)|^2$, where $STFT(\tau, \omega)$ is the Short-Time Fourier Transform of the time signal.

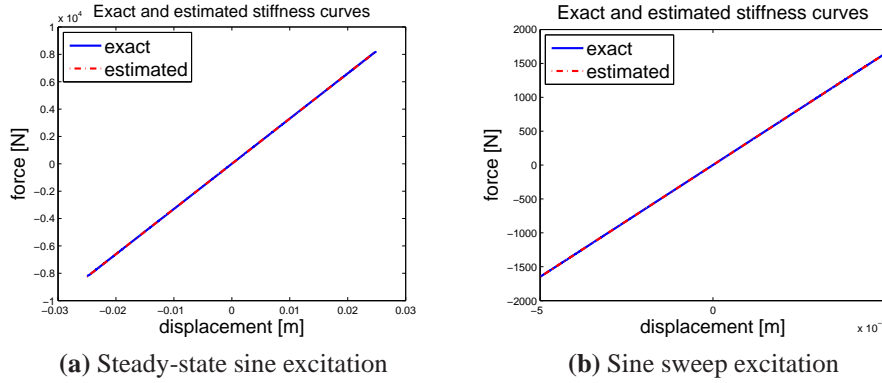


Figure 3.4: Exact and estimated stiffness curves - linear system

	k	c
exact parameters	330000	15
identified parameters (a)	330100	21
identified parameters (b)	329985	11

Table 3.1: Identification results for the linear case

3.4 Bilinear stiffness

The stiffness characteristic has the form

$$f_s(y) = \begin{cases} k_1 y & y < y_c, \\ k_2 y + (k_1 - k_2)y_c & y \geq y_c \end{cases} \quad (3.7)$$

The non-linear behaviour, which has been extensively studied in [29], can be seen by means of the homogeneity test only if $y_c \neq 0$, in fact, if $y_c = 0$ the equivalent non-linear stiffness (computed by means of the Harmonic Balance method, which is presented in Appendix A not to cause a digression here) is independent from the response amplitude and equals the average stiffness $\frac{1}{2}(k_1 + k_2)$ (as shown in Appendix A). If this happens, even though the force-displacement curve of the pure bilinear spring is non-linear, it will not cause distortions to the fundamental harmonic FRF. The system is thus homogeneous. This demonstrates that homogeneity is a necessary but not sufficient condition for linearity.

The same example simulated in [14] has been considered. It is described by the following equations

$$\begin{cases} 25\ddot{y} + 15\dot{y} + 330000y = p(t) & \text{if } y < 0.00072 \\ 25\ddot{y} + 15\dot{y} + 930000y = p(t) & \text{if } y \geq 0.00072 \end{cases} \quad (3.8)$$

The excitation signals are the one described for the linear case and shown in Fig.(3.2), the same can be said for the simulation time and the sampling frequency.

The results of this simulation are shown in Fig.(3.5),(3.6) and collected in Table (3.2). A piece-wise linear curve has been fitted to the data.

As can be seen, the exact parameters are not really well approximated in this case. This can be due to the fact that initial conditions are unknown and filtering using a cut-off frequency higher than 0 Hz imposes the filtered signal to be zero-mean, as explained in Section 2.2. As said, $\dot{y}(t)$ and $y(t)$ can be considered zero-mean signals under two conditions: $p(t)$ is a zero-mean sequence and the non-linear restoring force $f(y, \dot{y})$ is an odd function of its argument. This last condition is not satisfied for the bilinear stiffness and this leads to an inaccurate estimation of velocity and displacements.

Moreover, unlike what was done in the reference paper [14], where the clearance value was estimated separately from the stiffness values, here the clearance y_c has been included in the set of parameters to be estimated by curve-fitting the set of data, thus the optimization algorithm here used has to deal with three parameters (not two) at the same time.

	k_1	k_2	y_c
exact parameters	330000	930000	0.00072
identified parameters (a)	320312	893636	0.00053
identified parameters (b)	385566	891154	0.00078

Table 3.2: Identification results for the bilinear case

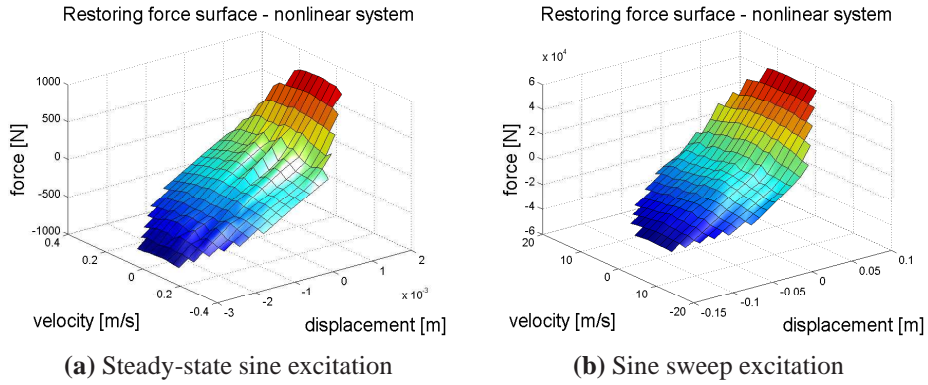


Figure 3.5: Restoring force surfaces - bilinear system

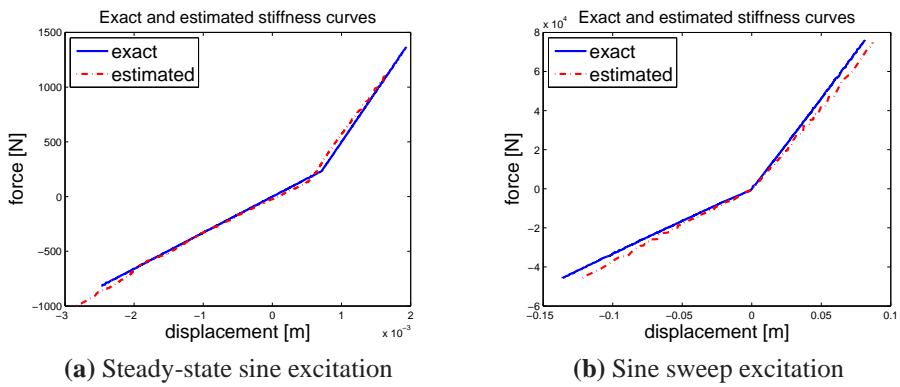


Figure 3.6: Exact and estimated stiffness curves - bilinear system

3.5 Non-linear damping

The most common form of polynomial damping is the quadratic one:

$$f_d(y) = c_2 \dot{y} |\dot{y}| \quad (3.9)$$

where the absolute value term is to ensure that the force is always opposed to the velocity.

The equation considered for the numerical simulation is the following

$$\ddot{y} + 30\dot{y} + 10\dot{y}|\dot{y}| + 1000y = p(t) \quad (3.10)$$

This system also has been tested considering two kinds of excitation signals, but with different parameters with respect to the previous cases.

For the steady-state excitation the equation is

$$p(t) = A \sin(\omega t)$$

where $A = 10000$ and ω is set equal to the system first natural frequency ($\simeq 31 \text{ rad/s}$).

The exponential sine-sweep is still described by equation (3.6), but with different parameters: the sweep rate is equal to 2 oct/min , the frequency range is 2-10 Hz.

The results of the simulation are shown in Fig.(3.7),(3.8) and collected in Table (3.3). A polynomial function of the form $c(x) = p_1 x^3 + p_2 x^2 + p_3 x + p_4$ has been fitted to the data.

	k	c (poly coeff.)			
		p_1	p_2	p_3	p_4
exact parameters	1000	0.2681	0	119.7	0.03
identified parameters (a)	1055	0.2048	-0.38	169.2	193.8
identified parameters (b)	1207	0.1694	0	170.2	-2.947

Table 3.3: Identification results for the non-linear damping case

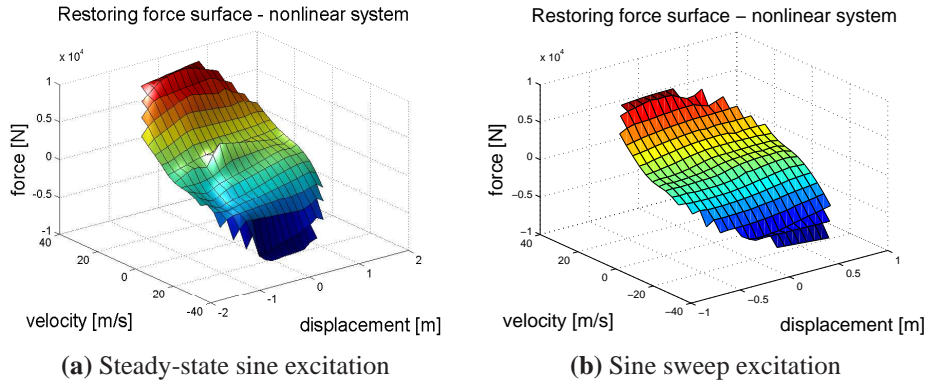


Figure 3.7: Restoring force surface - non-linear damping system

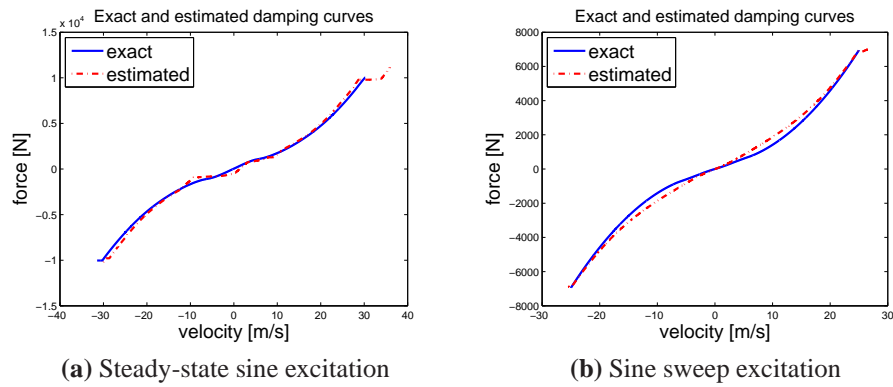


Figure 3.8: Exact and estimated damping curves - non-linear damping system

Chapter 4

FE modelling of a gap non-linearity

The aim of the first part of this chapter is to prove the usefulness of the Restoring Force Surface Method as a non-linearity identification tool also when more realistic structures are considered. For this purpose, a plate with a gap non-linearity has been modelled in Nastran and the Restoring Force Surface method has been subsequently applied on the resulting time histories.

In the second part of the chapter, a way to approximate the gap effect in a non-linear frequency response solution has been proposed.

Lastly, two methods for prescribing enforced motion in the non-linear solution sequences have been analysed and compared in view of what will be done in Chapter 6.

4.1 Linear plate analysis

The plate has dimensions $0.127 \times 0.0508 \times 0.0012 \text{ m}$ and, as shown in Fig.(4.1), it is constrained at nodes 1, 167 and 353. This constraints configuration has been chosen because it is similar to the one that characterize the structure in Chapter 6. The plate mass is 0.02145 kg .

The load is applied along the z -direction at node 32 and it is a sinusoid with unit amplitude and forcing frequency equal to the first natural frequency of the plate without the gap (therefore all six degrees of freedom at node 353 are constrained). The time response (SOL112) and the frequency response (SOL111)

are shown in Fig.(4.2) and their Nastran input files can be found in Appendix B. The first bending mode occurs at 79.26 Hz .

To define the benchmark for the stiffness parameters, two simulations have been run: one with node 353 fully constrained and one with node 353 free in the z -direction. In this way it is possible to determine the stiffness values (shown in Table 4.1) which represent the closed and the open gap conditions in such a way that $k_-, k_+ = k_{z,constrained}$ and $k = k_{z,free}$. Both linear simulations have been run using the modal transient solution sequence (SOL112) available in Nastran.

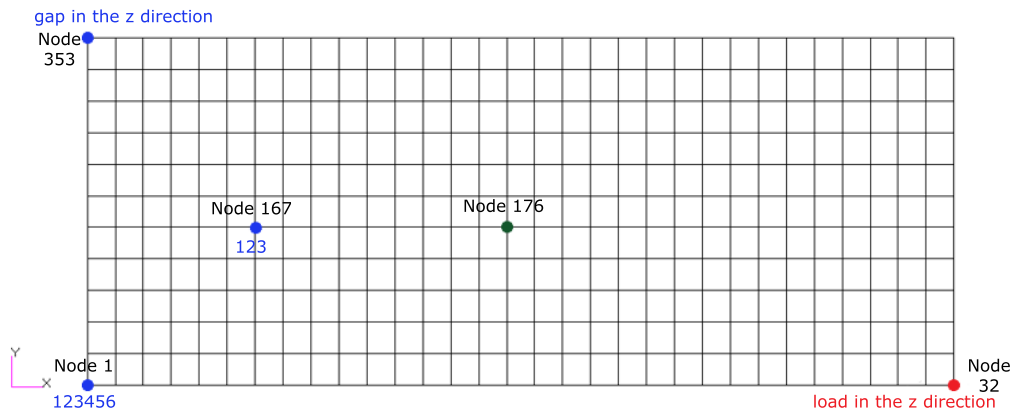


Figure 4.1: Plate FE model

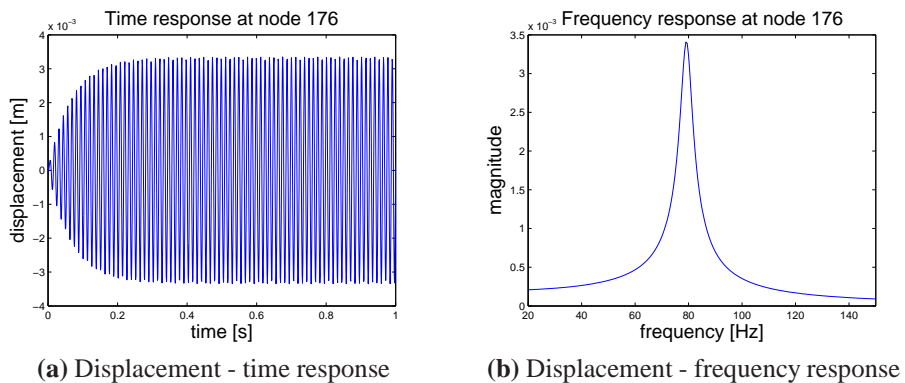


Figure 4.2: Plate dynamic responses

The Restoring Force Surface method applied to the simulated linear plates yields the results shown in Fig.(4.3) and in Fig.(4.4). To check the stiffness values

$k_{z,constrained}$	5318.6 N/m
$k_{z,free}$	3592.4 N/m

Table 4.1: Stiffness parameters benchmarks

found by curve fitting the data, the stiffness can be computed as $k = \omega^2 m$ which yields a value of 5319.8 N/m.

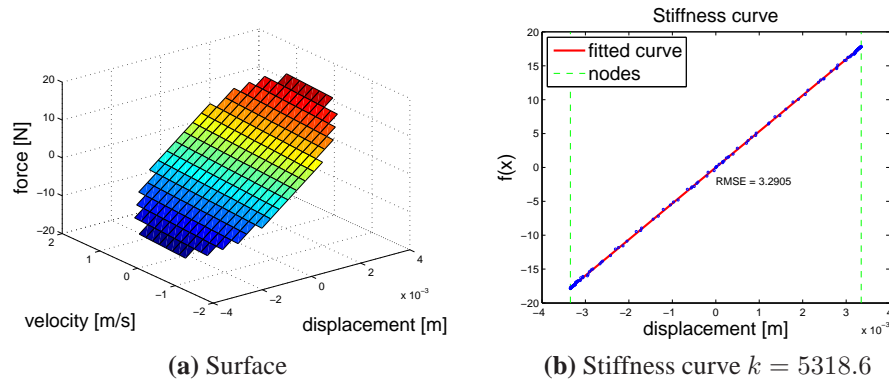


Figure 4.3: RFS - linear plate (node 353 fully constrained)

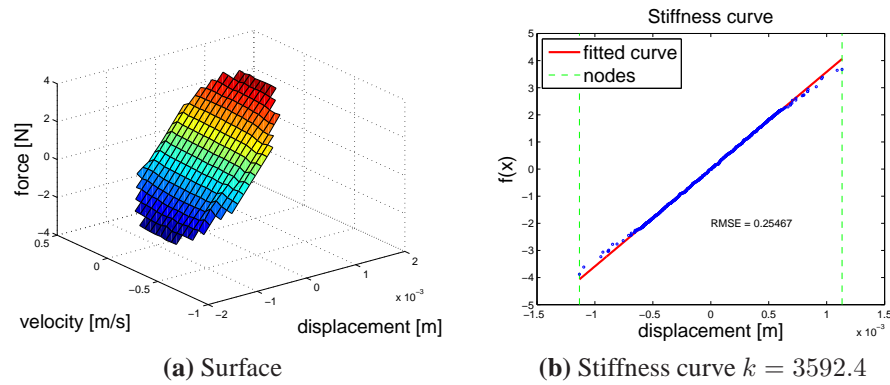


Figure 4.4: RFS - linear plate (node 353 free in the z direction)

4.2 Gap modelling and non-linear parameters identification

The symmetric gap has been modelled by means of the CGAP and PGAP cards [30], which are intended, among the others, for the non-linear solution sequence 129.

The simulation parameters have been chosen as follows:

- to determine the value of the axial stiffness of the closed gap, a linear spring along z has been introduced at node 353 and its value has been set equal to $10^9 N/m$ to simulate the constraint. The simulation has been run using SOL112 and the result has been compared with the one obtained substituting the spring with an actual constraint to make sure they were equal.
- the same model has been run with a SOL129 to check the correctness of the PARAM,W4 value (SOL129 is a direct solution, therefore does not allow to define the damping using the TABDMP1 card in which it is specified as percentage of the critical damping).
- the initial gap opening has been chosen looking at the displacement at node 353 obtained from the simulation run without the z constraint (Fig. 4.5). The chosen value is $4 \cdot 10^{-4} m$.
- the axial stiffness for the open gap has been set equal to $10^{-6} N/m$.

The setup of the non-linear transient analysis is shown in Listing(4.1).

For all the simulations the time step size has been chosen taking into consideration the frequency content of the input load and the frequency of the mode of interest (the first one only). In SOL129 the only method allowed for the integration scheme is ADAPT: the program automatically adjusts the incremental time, which also means that the number of time steps will not be equal to the one defined in the card. The user-defined Δt is used as an initial value for the time step size [31].

4.2. GAP MODELLING AND NON-LINEAR PARAMETERS IDENTIFICATION 33

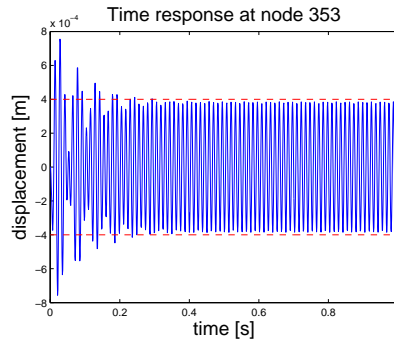


Figure 4.5: Time response at node 353 when the z dof is left free

In order to have a better coverage of the phase-plane, the outputs of the simulation have been resampled at a constant sampling frequency of 10 kHz .

The application of the identification method produced the results in Fig.(4.6) and collected in Table (4.2). Since the stiffness is piece-wise linear, a non-polynomial model expressed by equation(4.1) has been fitted to the data.

$$f_s(y) = \begin{cases} k_+y + (k - k_+)y_c & y > y_c, \\ ky & |y| \leq y_c \\ k_-y + (k - k_-)y_c & y < -y_c \end{cases} \quad (4.1)$$

	k_-	k	k_+	y_c	y_c
exact parameters	5318.6	3592.4	5318.6	-0.0004	0.0004
identified parameters	6657.3	4540.3	6751.5	-0.000419	0.000436

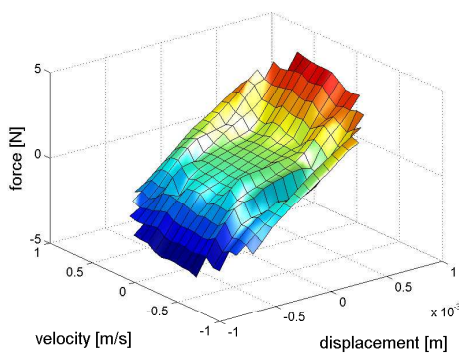
Table 4.2: Symmetric gap identified parameters

Listing 4.1: SOL129 - symmetric gap

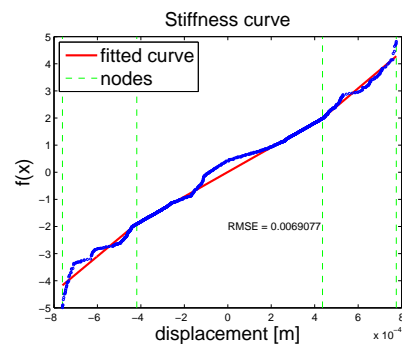
```

SOL 129
$ Case
TSTEPNL = 1
$
$ Bulk
PARAM W4 498.
$
$TSTEPNL ID NDT DT NO METHOD KSTEP MAXITER CONV
TSTEPNL 1 10000 1.5-3 1 ADAPT 2 10 PW
$
$ Material
$MAT1 MID E G NU RHO A TREF GE
MAT1 1 7.0E+10
$
$ Gap
$PGAP PID U0 F0 KA KB KT MU1 MU2
$ TMAX MAR TRMIN
PGAP 889 4.-4 0. 1.+9 1.-6 1.+8
1.2-4
$CGAP EID PID GA GB X1 X2 X3 CID
CGAP 888 889 353 998 1. 0. 0.
CGAP 887 889 997 353 1. 0. 0.
$ x,y coordinates equal to x,y coordinates of grid 353
GRID* 998 0. .050799999386072
* 0.001
GRID* 997 0. .050799999386072
* -.001

```



(a) Surface



(b) Stiffness curve

Figure 4.6: Restoring force surface symmetric gap

4.3 Sine-sweep excitation

The verification of the mathematical model used in forced frequency response predictions is usually carried out by means of shaker-vibration sine tests, therefore two ways to set up the numerical analysis under a sine-sweep excitation will be discussed in the following.

The easiest method to be implemented requires the use of the TLOAD1 card together with the TABLED1 card, which allows the definition of a tabular function to generate a time-dependent dynamic load. In this way it is still possible to run a transient analysis (SOL129) and the gap non-linearity is modelled as explained earlier.

To generate the tabular values to be used in the analysis, equations (3.1) and (3.4) have been implemented in MATLAB. The frequency range $50 - 100 \text{ Hz}$ has been swept at $4 \text{ oct}/\text{min}$. The total duration of the simulation is therefore of 15 s . The load has been applied at node 32, as before.

Care must be applied in the definition of the starting and ending frequency for this kind of analysis, in fact, the frequency range to be swept should be chosen as small as possible in order to reduce the computation time especially when running the non-linear solution sequence.

The first simulation that has been run is the linear one (SOL109) and the resulting acceleration is shown in Fig.(4.7a). Then the non-linear simulation sequence SOL129 has been run and the resulting acceleration (Fig. 4.7b) clearly shows the so called *jump phenomenon*¹ caused by the presence of the non-linearity.

The results obtained applying the Restoring Force Surface method to the non-linear time histories are shown in Fig.(4.8) and collected in Table(4.3).

During tests the input excitation is usually given as enforced acceleration, therefore it is useful to analyse the methods available in the Nastran different solution sequences. The enforced motion analysis set-up will be discussed in depth in Section 4.5. The concepts there explained will be then applied in

¹Jump phenomena are caused by small variations of the initial conditions of the motion which may drift the response between competing domains of attraction of stable solutions in the phase space of the system.

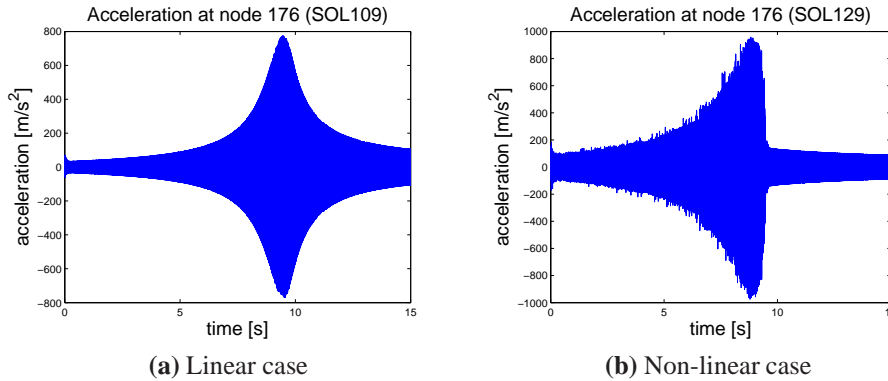


Figure 4.7: Acceleration at node 176 (\approx CoG) - input given as LOAD

	k_-	k	k_+	y_c	y_c
exact parameters	5318.6	3592.4	5318.6	-0.0004	0.0004
identified parameters	5196.5	3939.7	5188.3	-0.000414	0.000414

Table 4.3: Symmetric gap identified parameters under sine-sweep excitation

Chapter 6.

The computational time of the transient solutions grows as the size of the model increases and might become prohibitive for very large models. For this reason, an alternative method to simulate the non-linear response of the structure to a sinusoidal excitation will be presented. In Nastran the Non-linear Harmonic Response solution (SOL128) allows to run the analysis directly in the frequency domain where the sinusoidal excitation, defined in a given frequency range, can

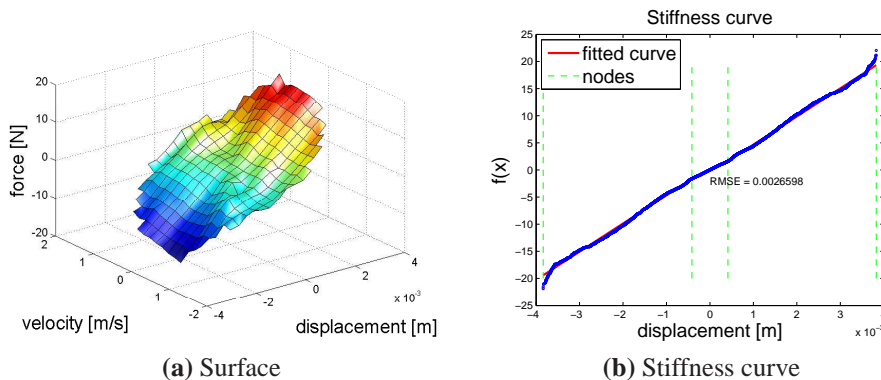


Figure 4.8: Restoring force surface - sine-sweep excitation

be easily defined by means of the RLOAD2 card. The application of this second method showed a big improvement in terms of computational time and therefore it will be explained in details in Section 4.4.

4.3.1 Comparison with SOL400

As stated in [31], the solution sequence SOL129 is the preferred one when dealing with transient response analysis in the presence of non-linearities. As a comparison, the previous analysis has been run using the implicit non-linear solution sequence SOL400.

The acceleration obtained running the SOL400 is shown in Fig.(4.9) and can be compared with the one obtained running the SOL129 (Fig. 4.7b). Since the two input files are identical, the difference in the two responses (one being more noisy than the other) could be addressed to the algorithms implemented in the solution sequences not being the same. The differences reduce when considering velocities (Fig. 4.10) and displacements (Fig. 4.11).

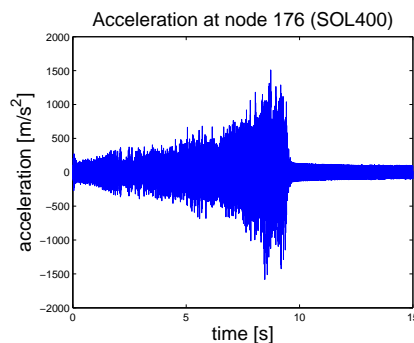


Figure 4.9: Acceleration (SOL400)

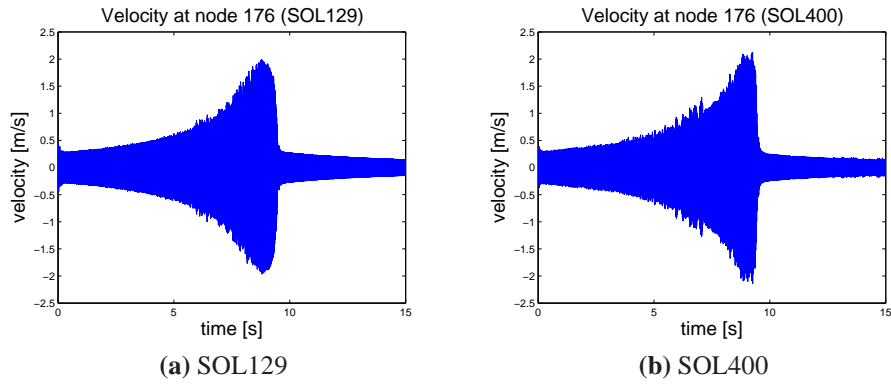


Figure 4.10: Velocities comparison

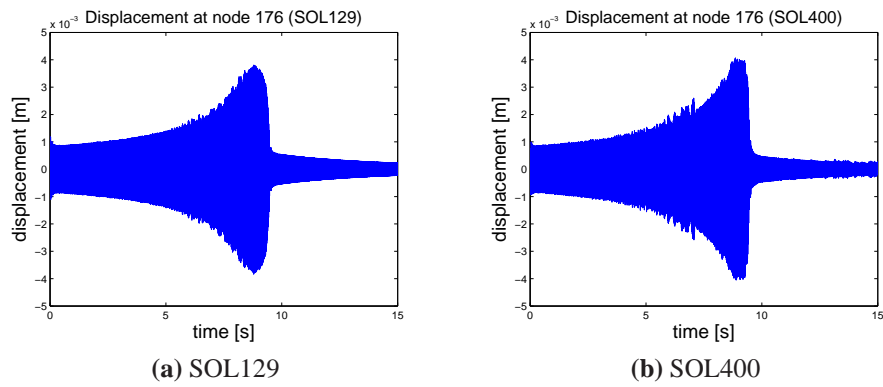


Figure 4.11: Displacements comparison

4.4 Non-linear harmonic response

A non-linear harmonic response solution (SOL128) is available in Nastran and it allows the analysis of the dynamic response of non-linear structures which exhibit a periodic response when subjected to a harmonic excitation. This means that the degree of non-linearity in the system has to be light enough that the response can be described as a combination of harmonic responses through the Harmonic Balance Method (see Appendix A for a full explanation of the method).

The Harmonic Balance Method assumes the steady-state response consists of a sum of sinusoidal responses and therefore it can be efficient only if a small number of sinusoids is necessary to approximate the solution. Its limitation is that it can only capture harmonic components, so any frequency which is not a pure sub- or super-harmonic² of the excitation will be lost.

The main issue related to this solution is convergence. Non-convergence can be attributed to dynamically unstable conditions, to the reaching of a bifurcation or turning point or to an insufficient number of harmonics taken into account. In the case of non-convergence, the response quantities are set to zero and the calculation continues to the next excitation frequency retaining the initial conditions of the solution from the last converged frequency.

Since the CGAP card is no more available in this solution sequence³, non-linearities have to be defined as non-linear dynamic forces formulated using NOLINi entries, which describe the force as a function of displacement.

As said, the non-linearities in the system must be mild to achieve convergence, therefore the model for the gap non-linearity needs to be adjusted not to have an abrupt change in slope of the force-displacement curve, because it will cause convergence difficulties. In fact, if the stiffness undergoes to sudden changes to simulate a hard contact, higher order harmonics will be generated and therefore it is no more true that the response can be approximated by a small number of

²Super-harmonic responses represent permanent oscillations whose frequencies are multiple of the forcing frequency.

³It has to be noted, however, that it is possible to define a non-linear radial gap both in the non-linear transient and in the non-linear harmonic responses by means of the NLRGAP card. Differently from the CGAP card, which defines an element, the NLRGAP defines a non-linear load similar to the NOLINi Bulk Data entries.

sinusoids, as requested by the solution sequence. However, it can be reasonable to assume that the change in stiffness will be smoother in practice than for numerical example.

For these reasons, the stiffness curve which represents the clearance non-linearity has been approximated using a polynomial model of the form $p(x) = p_1 x^3$, as shown in Fig.(4.12). The polynomial coefficient p_1 is estimated to be equal to $1.77 \cdot 10^9$. This value will be used to model the non-linear input defined by the cards NOLIN3 and NOLIN4.

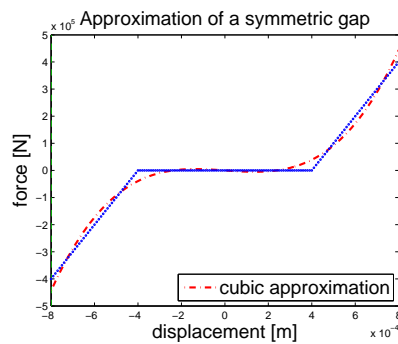


Figure 4.12: Polynomial approximation of the gap

The starting point for the setup of this analysis is the linear direct frequency response (SOL108). The changes needed for the SOL128 are shown in Listing(4.2).

The simulation has been run for four different load levels: $0.1 N$, $1 N$, $10 N$ and $100 N$. The results are then compared with the results obtained running the transient analysis (SOL129) introduced in Section 4.2.

As can be seen from Fig.(4.13) to (4.17) the effect of the approximation introduced in Fig.(4.12) is translated into a different response amplitude in the two cases, the error being more severe when the level of the input excitation is an intermediate value between the two limit conditions: always open gap and always closed gap.

At the first load level of $0.1 N$ (Fig. 4.13a), the structure behaves like if the z degree of freedom (dof) at node 353 was not constrained (Fig. 4.14). This happens because the load is too low to activate the non-linearity.

Since the response in Fig.(4.14) was obtained running a linear frequency

Listing 4.2: SOL128 analysis set-up

```

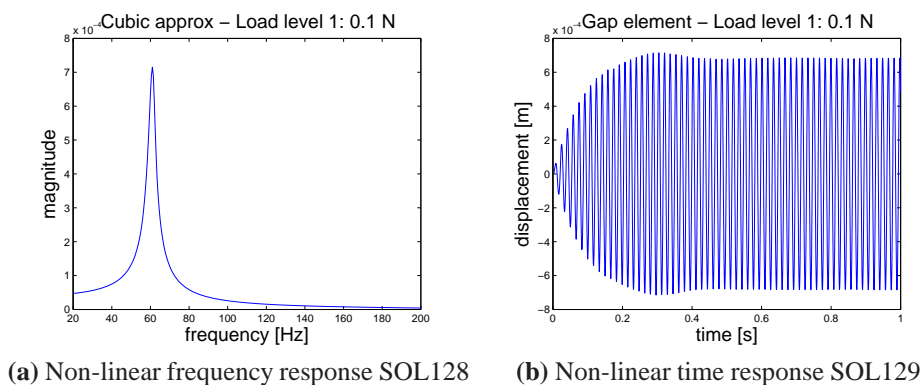
SOL 128
$ Case
NLHARM = 100
NONLINEAR = 111
$
$ Bulk
$NLHARM ID      SUBFAC  NHARM  NLFREQ
NLHARM  100     1        5      101
$
$ Spin up
$NLFREQ1 ID     F1      DF      NDF
NLFREQ1 101    20     .5     360
$
$ Cubic nonlinear stiffness
$ Tension
$NOLIN3 SID     GI      CI      S      GJ     CJ     A
NOLIN3  111    353    3      -1.77E+9 353   3     3.
$ Compression
NOLIN4  111    353    3      -1.77E+9 353   3     3.

```

response (SOL111) with a unit amplitude input excitation, care must be taken when choosing the level of the input excitation, because there is no perfect equivalence in the output responses.

When the load level increases (Fig 4.17), the non-linearity is always active, therefore it behaves as a constraint and the response is similar to the one obtained with the actual constraint (Fig. 4.18).

The homogeneity test shown in Fig.(4.19) highlights the presence of the non-linearity and its effects on the natural frequency of the plate.

**Figure 4.13:** Response comparison for load level 1: 0.1 N

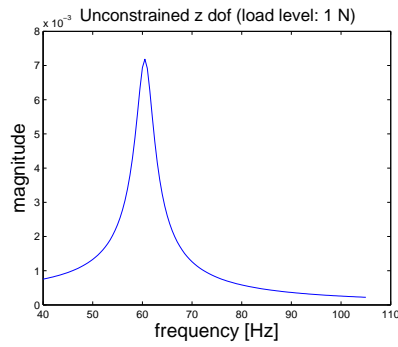
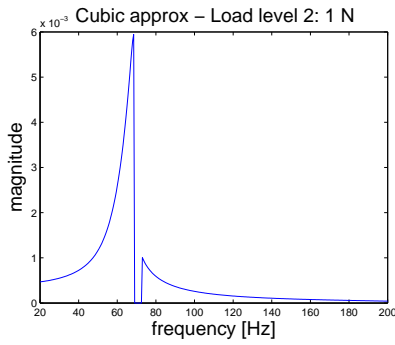
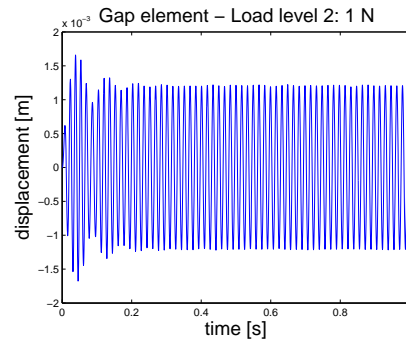


Figure 4.14: Linear frequency response for unconstrained z dof at node 353 ($f_n = 60.54 \text{ Hz}$)

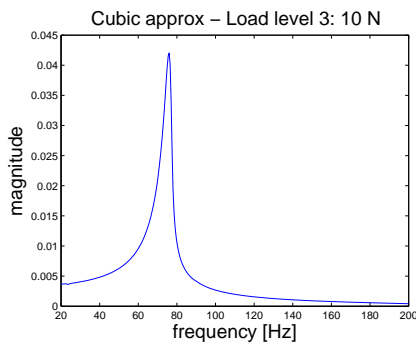


(a) Non-linear frequency response SOL128

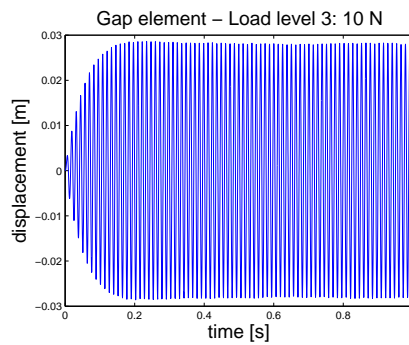


(b) Non-linear time response SOL129

Figure 4.15: Response comparison for load level 2: 1 N



(a) Non-linear frequency response SOL128



(b) Non-linear time response SOL129

Figure 4.16: Response comparison for load level 3: 10 N

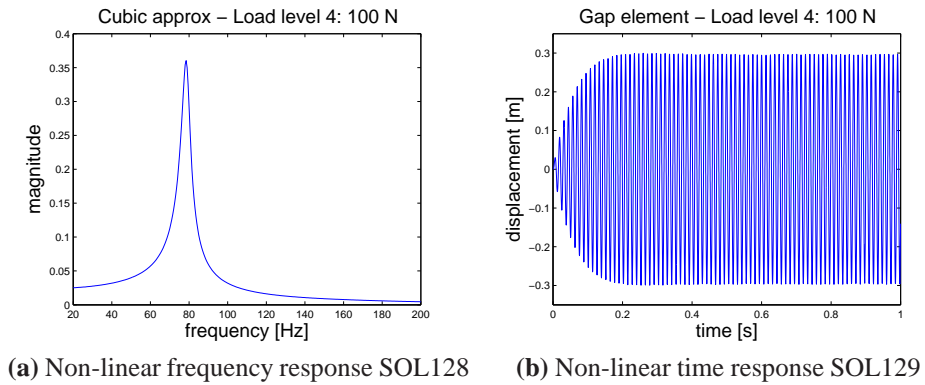


Figure 4.17: Response comparison for load level 4: 100 N

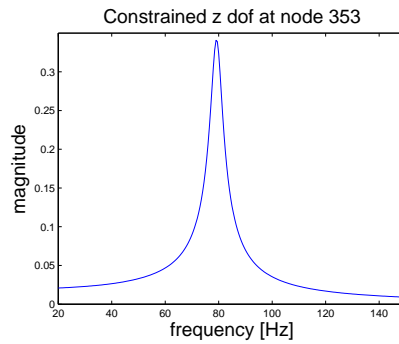


Figure 4.18: Frequency response when the z dof at node 353 is constrained ($f_n = 79.26 \text{ Hz}$)

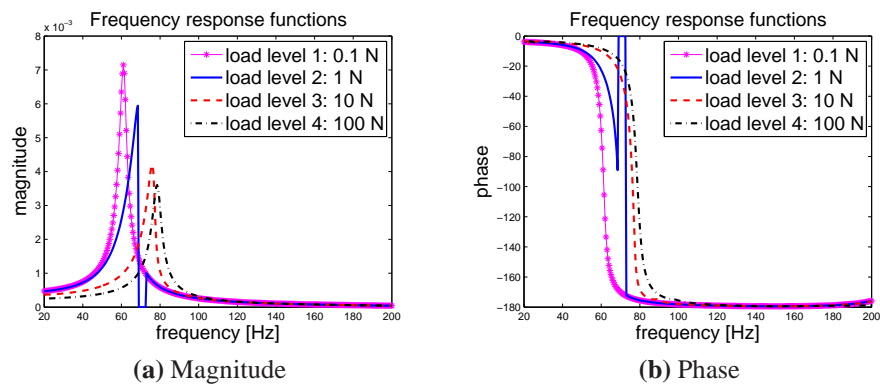


Figure 4.19: Frequency response functions for different load levels (homogeneity test)

4.5 Enforced acceleration

Enforced motion can be used to specify accelerations at a set of grid points for frequency and transient response.

In Nastran, two main methods are available to specify motion: the Direct Enforced Motion (DEM) and the Large Mass Method (LMM). The first one allows direct specification of displacements, velocities or accelerations via the SPC and SPCD data entries; the second one is implemented by placing large masses on all enforced degrees of freedom and supplying dynamic loads specified by equation (4.2).

$$p = m_0 \ddot{u} \quad (4.2)$$

The mass should be at least 10^6 times the mass of the entire structure for an enforced translational dof, keeping in mind that the accuracy of the approximation increases as m_0 is made larger.

Since these two methods are implemented in different solution sequences, the choice of the method to be used in the analysis is driven by the kind of solution sequence that needs to be run. The Direct Enforced Motion is implemented in direct and modal frequency analysis (SOL108 and SOL111), direct and modal transient analysis (SOL109 and SOL112) and in the non-linear solutions SOL400 and SOL128. The Large Mass Method is applicable to both transient response and frequency response and it is the only method available to prescribe enforced motion in SOL129.

The set-ups of both analysis are presented in Listing(4.3) and Listing(4.4). The motion has been enforced at node 167 in the z -direction.

When implementing the Direct Enforced Motion via SPCD card, the components specified in SPCD data must be also referenced on SPC or SPC1 entries (which means that defining a SPCD for one dof implies constraining that dof).

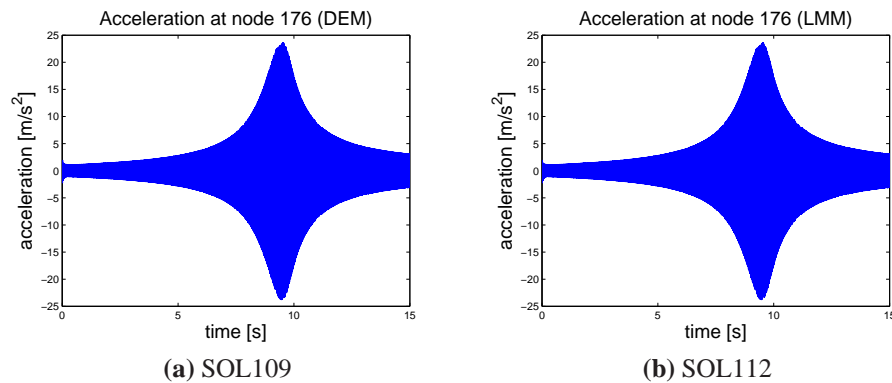
The results obtained running the Direct Enforced Motion in SOL109 and the Large Mass Method in SOL112 are presented in Fig.(4.20).

Listing 4.3: SOL109 Direct Enforced Motion

```

PARAM  ENFMETH REL
PARAM  ENFMOTN REL
$
$ Constraints
SPCADD 2      1      996
SPC1   1      123456 1      353
SPC1   996    123    167
$
$ Dynamic loading
$DLOAD SID    S      S1     L1
DLOAD  2      1.     1.     88
$TLOAD1 SID    EXCID  DELAY  TYPE  TID    US0    VS0    P
TLOAD1 88      99      ACCE   77    0.     0.
$
$SPCD  SID    G1     C1     D1
SPCD   99     167    3      1.

```

**Figure 4.20:** Comparison between accelerations obtained by means of DEM (SOL109) and LMM (SOL112)

As can be seen, the responses are virtually the same provided that

- the rigid body modes are removed by means of the PARAM,LFREQ parameter in SOL112, so doing the responses are relative to the overall motion of the structure and are not absolute quantities
- only the dynamic enforced motion solution relative to the static-based solution is taken into account in SOL109 by means of the PARAM,ENFMOTN and PARAM,ENFMETH parameters

When moving to the non-linear solution sequences, the aforementioned parameters are no more available. This means that the displacement will be

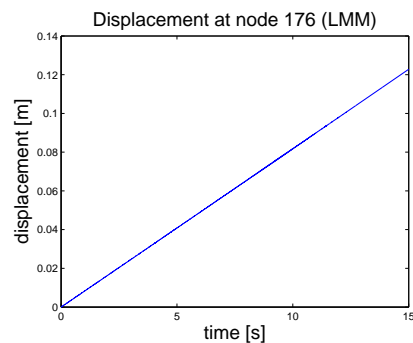
Listing 4.4: SOL112 Large Mass Method

```

EIGRL      1      -0.1    3000.      0
$ Discard rigid body mode
PARAM     LFREQ    0.1
$
$ Large mass
$CMASS1   EID      PID      G1      C1
CMASS1    555      554      167     3
PMASS     554      1.+9
$
$ Constraints
SPCADD    2        1        999     996
SPC1      1        123456   1       998     997
SPC1      999     12456   353
SPC1      996     12       167
$
$ Dynamic loading
$DLOAD    SID      S        S1      L1
DLOAD     2        1.       1.     88
$TLOAD1   SID      EXCID   DELAY   TYPE   TID    US0    VS0    P
TLOAD1    88      99
$
$DAREA    SID      P1      C1      A1
DAREA     99      167     3       1.+9

```

affected by rigid-body drift, i.e. it increases continuously with time, as shown in Fig.(4.21). As a consequence, the only way to obtain the relative responses is to post-process the time histories (integration and filtering of the relative acceleration response to obtain relative velocity and displacement). Being the structure non-linear, the principle of superposition does not hold any more, therefore, to be able to retrieve the relative responses, the motion must be enforced at one dof only.

**Figure 4.21:** Effect of the rigid-body drift on the displacement

The acceleration response obtained by means of the Large Mass Method

implemented in the non-linear solution sequence SOL129 is shown in Fig.(4.22). Again, the *jump phenomenon* reveals the presence of the non-linearity.

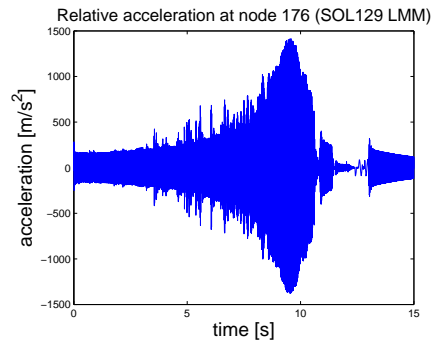


Figure 4.22: Relative acceleration obtained running the LMM in SOL129

Chapter 5

Experimental study of a piecewise linear beam

Until now, the Restoring Force Surface method has been tested on numerical examples only. To move a step forward toward the identification of a real system, a simple experimental case has been prepared in order to apply the method to a real, but controlled, configuration (similar to the one tested in [4]).

The tested system is a beam made of aluminium, mounted horizontally with one clamped end and one free end, as shown in Fig.(5.1). The dimension and material constants for the beam are given in Table (5.1).

If the amplitude of the transverse motion exceeds a fixed limit, the beam makes contact with two stops. In the experiment here described, the clearance was set at 3.56 mm . When the beam makes contact with the stops, its effective length is lowered with a consequent rise in stiffness. Therefore, for transverse vibrations, the beam has a piecewise linear stiffness. Separate tests were carried out at low and high excitation.

Top view

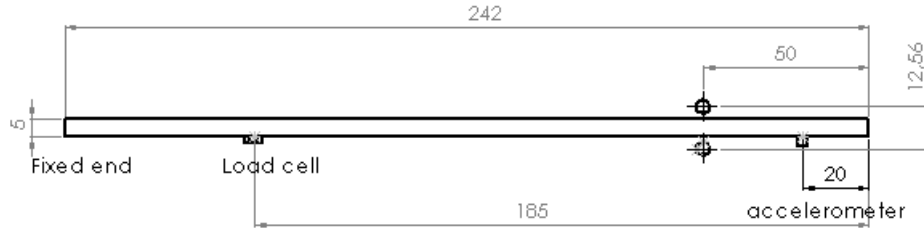


Figure 5.1: Beam test set-up

Length, L	242 mm
Width, w	30 mm
Thickness, t	5 mm
Density, ρ	2720 kg/m ³
Young's modulus, E	70 · 10 ⁹ N/m ²
Second moment of area, I	3.125 · 10 ⁻¹⁰ m ⁴
Mass per unit length, m_l	0.4563 kg/m

Table 5.1: Dimensions and material constants for cantilever beam

5.1 Low excitation test

The behaviour of the beam without impacts should be the one of a linear system and therefore it can be compared with theory. According to [32], the first two natural frequencies of a cantilever (fixed-free) beam are

$$f_i = \frac{\lambda_i^2}{2\pi L^2} \sqrt{\frac{EI}{m_l}} \text{ Hz} \quad (5.1)$$

where $\lambda_1 = 1.87510407$, $\lambda_2 = 4.69409113$ and $I = wt^3/12$. This gives theoretical natural frequencies of 70.3 Hz and 440.6 Hz. From a first test the identified frequencies are 61.5 Hz and 359 Hz. This underestimate is due to the additional mass loading caused by the presence of the accelerometer and of the load cell, since their mass is the 12% of the beam mass.

The theoretical stiffness for the beam can be estimated from theory. Applying a unit load at a distance a from the free-end, the equation for the elastic curve can

be written as

$$EI \frac{d^2 y}{dx^2} = M(x) \quad (5.2)$$

The bending moment has the form $M(x) = \langle x - a \rangle$ where $\langle \dots \rangle$ is the Macaulay's bracket which vanishes if the argument is negative.

Integrating twice and applying the boundary conditions for the clamped end (the complete derivation can be found in Appendix C) the displacement is

$$y(x) = \frac{1}{6EI} [\langle x - a \rangle^3 - 3(L - a)^2 x + 3(L - a)^2 L - (L - a)^3] \quad (5.3)$$

Evaluating equation(5.3) at a distance d , it is then possible to compute the observable stiffness for the accelerometer as $k_d = 1/y(d) = 66333 \text{ N/m}$.

The mass m_d is fixed, once the natural frequency of the system is known, by the relation

$$m_d = \frac{k_d}{\omega_n^2} \quad (5.4)$$

The first two modes are well separated and the first mode is the bending mode, therefore, if only the first mode is excited, the beam is assumed to behave as a SDOF system described by the following equation (where d is the position of the measurements devices)

$$m_d \ddot{y}(d) + c_d \dot{y}(d) + k_d y(d) = p(t) \quad (5.5)$$

Having made this assumption, the beam was excited with a stepped-sine sequence band-limited in the 55 – 70 Hz range (Fig. 5.2). The shaker is attached to the beam by a stinger. Both the acceleration and displacement responses (Fig. 5.3) have been measured and the data have been acquired with a sampling frequency set to 200 Hz .

In this case, the velocity could be obtained in two ways:

- integrating it from the acceleration and high-pass filtering to eliminate spurious components from the integration, as discussed in Section 2.2
- it could be estimated by means of a Kalman filter using both the acceleration and the displacement measurements.

The second approach was already used in [7], but with a different formulation with respect to the one presented in this thesis. The complete formulation is given in Section 5.3.

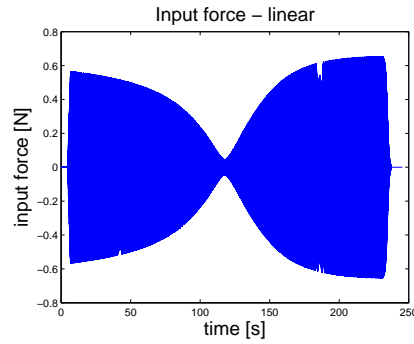


Figure 5.2: Force time history - linear test

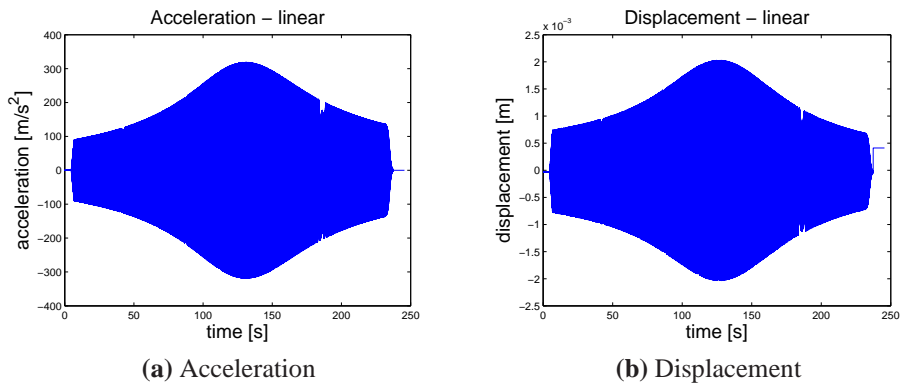


Figure 5.3: Measured responses - linear test

Once the velocity has been obtained applying one of the two methods mentioned earlier, the Restoring Force Surface method can be applied. For the linear beam, it yields the surface and stiffness curve shown in Fig.(5.4). The estimated stiffness is $k_{est} = 63014 \text{ N/m}$.

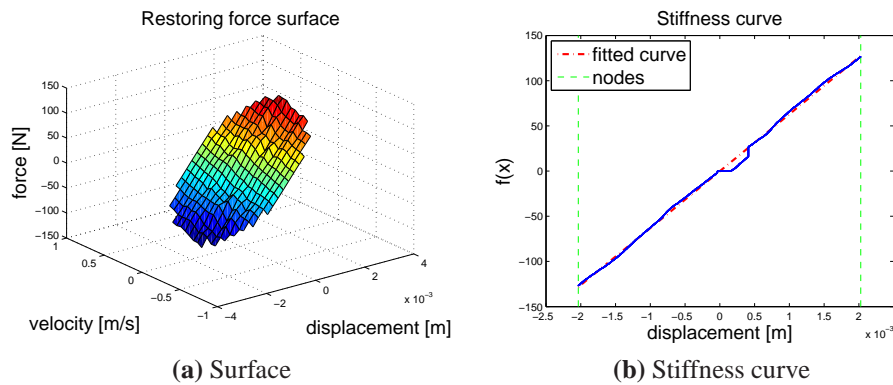


Figure 5.4: Restoring Force Surface method applied to the linear beam

Subsequently, the test has been carried out at four different levels of excitation to activate the non-linearity. As the level of excitation increases, the non-linear behaviour becomes more visible, as shown by the homogeneity test in Fig.(5.5).

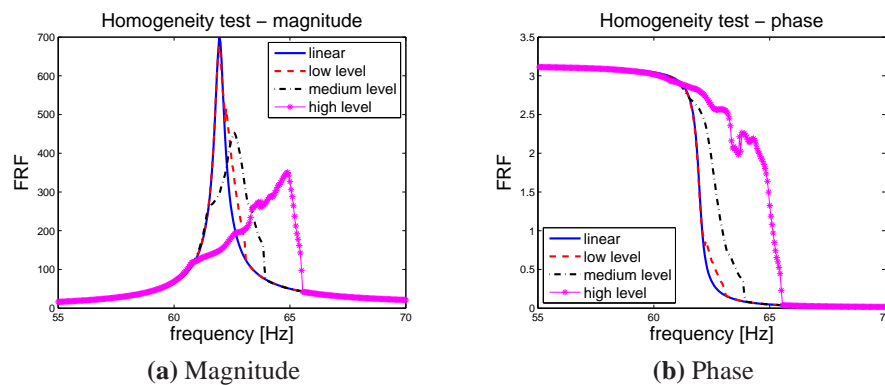


Figure 5.5: Homogeneity test for the cantilever beam

5.2 High excitation test

Being the effect of the non-linearity more evident at high level of excitation, the parameters identification technique has been applied to the responses obtained at the highest level of excitation tested.

The input sequence is shown in Fig.(5.6), whereas the time histories of acceleration and displacement are shown in Fig.(5.7), where the *jump*

phenomenon is now visible although not really clear-cut (it was not possible, with this set-up, to make it more clear without overloading the shaker).

The Restoring Force Surface method applied to the non-linear test responses yields the results shown in Fig.(5.8) and collected in Table (5.2). The identified parameters show good agreement with the theoretical ones and this proves that the Restoring Force Surface method is an useful tool for identifying real systems.

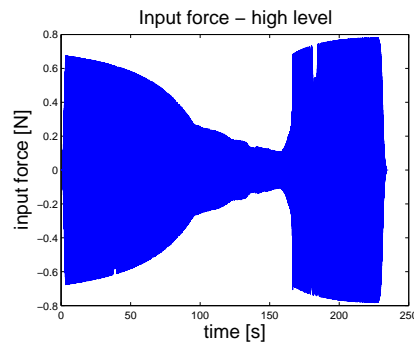


Figure 5.6: Force time history - high excitation test

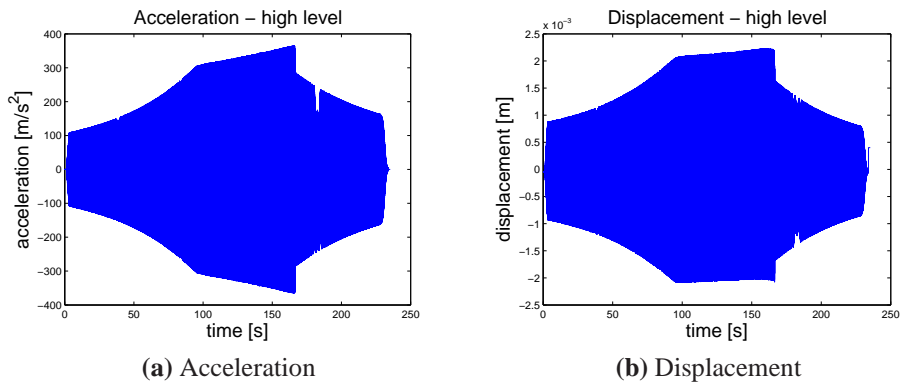


Figure 5.7: Measured responses - high excitation test

	k_-	k	k_+	y_c	y_c
exact parameters	74098	66333	74098	-0.00178	0.00178
identified parameters	70152	63166	74852	-0.00189	0.0018

Table 5.2: Identified parameters for non-linear beam

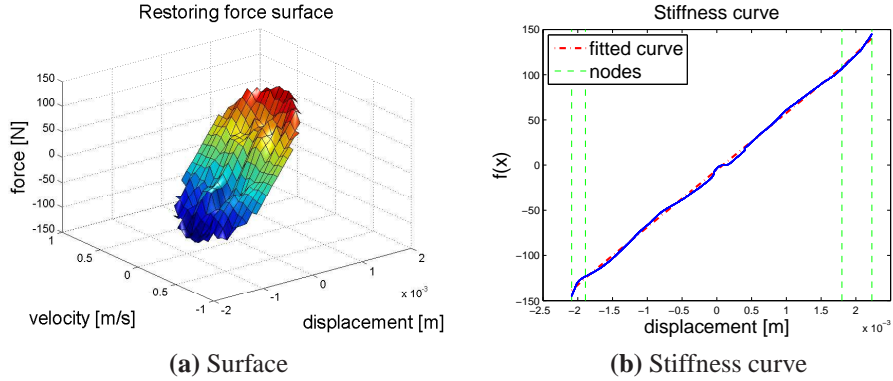


Figure 5.8: Restoring Force Surface method applied to the non-linear beam

5.3 Velocity estimation via Kalman filter

An exhaustive introduction to the Kalman filter can be found in the original paper published by Kalman [33] and in Welch and Bishop paper [34], whereas here only the information needed for the filter set-up will be discussed.

The Kalman filter tries to estimate the state of a discrete-time process governed by the following equations ¹:

$$\mathbf{x}_k = \mathbf{A}\mathbf{x}_{k-1} + \mathbf{q}_{k-1} \quad (5.6a)$$

$$\mathbf{z}_k = \mathbf{H}\mathbf{x}_k + \mathbf{r}_k \quad (5.6b)$$

where \mathbf{x} is the state vector, \mathbf{A} is the state transition matrix, \mathbf{z} is the vector of measurements and \mathbf{H} is the observation matrix. The random variables \mathbf{q}_k and \mathbf{r}_k represent the process and measurement noise respectively and they are assumed to be independent of each other, white and with normal probability distributions given by

$$p(\mathbf{q}) \sim N(0, \mathbf{Q})$$

$$p(\mathbf{r}) \sim N(0, \mathbf{R})$$

¹In the original equations presented by Kalman in [33] there was also a term $\mathbf{B}u$, which is added to equation (5.6a) and represents the input to the system. This term is here omitted because there is no input term in equations (5.7)

where \mathbf{Q} is the process noise covariance matrix and \mathbf{R} is the measurement noise covariance matrix. The process noise serves the purpose of taking into account all the factors that influence the system and that are not known and/or modelled.

The state vector \mathbf{x} and the matrix \mathbf{A} can be written by considering the equations that describe the system, which are:

$$p_k = p_{k-1} + \Delta t v_{k-1} + \frac{\Delta t^2}{2} a_{k-1} \quad (5.7a)$$

$$v_k = v_{k-1} + \Delta t a_{k-1} \quad (5.7b)$$

$$a_k = a_{k-1}; \quad (5.7c)$$

where p , v and a represent position, velocity and acceleration respectively. Therefore, $\mathbf{x} = [p \ v \ a]^T$ and \mathbf{A} takes the form:

$$\mathbf{A} = \begin{bmatrix} 1 & \Delta t & \frac{\Delta t^2}{2} \\ 0 & 1 & \Delta t \\ 0 & 0 & 1 \end{bmatrix}$$

Since the measured quantities are acceleration and displacement, the observation matrix \mathbf{H} takes the form:

$$\mathbf{H} = \begin{bmatrix} 1 & 0 & 0 \\ 0 & 0 & 1 \end{bmatrix}$$

The matrix \mathbf{R} can be obtained by taking some off-line sample measurements and computing the variance of the measurement noise.

The matrix \mathbf{Q} , instead, needs a special attention. In fact, typically there is not the possibility to directly observe the process that needs to be estimated, therefore the determination of \mathbf{Q} usually follows from an off-line tuning process, keeping in mind that it must satisfy the properties of a covariance matrix, which means it must be symmetric and positive-semidefinite².

Since the effect of \mathbf{Q} is to increase the uncertainty of the prediction, it is

²A matrix is said to be positive-semidefinite if $\mathbf{x}^* \mathbf{M} \mathbf{x} \geq 0$ for all \mathbf{x} in \mathfrak{R}^n . A quick check could be performed computing all the eigenvalues, which have to be non-negative, of the Hermitian part $\frac{\mathbf{M} + \mathbf{M}^T}{2}$.

possible to define some guidelines for the choice of \mathbf{Q} :

- huge values (compared to \mathbf{P} , which will be introduced later on in the section) means that the model does not predict the process accurately enough; if \mathbf{Q} is too large, then the filter will be too much influenced by the noise in the measurements
- low values of \mathbf{Q} indicate confidence that any unknown noise term and/or modelling error is small, but the filter may become overconfident in its estimate of the state which could diverge from the actual solution

In this case the process noise covariance matrix is the following

$$\mathbf{Q} = \begin{bmatrix} 2e6 & 5e7 & 0 \\ 5e7 & 8e9 & 5e3 \\ 0 & 5e3 & 2e6 \end{bmatrix}$$

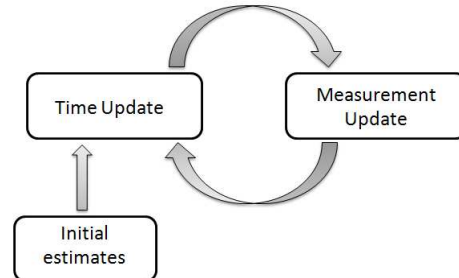


Figure 5.9: The discrete Kalman filter loop

Now that all the elements have been defined, the discrete Kalman filter can be implemented (the complete code can be found in Appendix D). The Kalman filter works in two steps (Fig. 5.9):

1. Time update: the current state and error covariance estimates are projected forward in time to obtain the a priori estimates for the next time step.
2. Measurement update: a new measurement is incorporated into the a priori estimate to obtain an improved a posteriori estimate.

The equations have to be implemented according to the following scheme, as explained in [34]:

1. Time update

- (a) Project the state ahead

$$\hat{\mathbf{x}}_k^- = \mathbf{A}\hat{\mathbf{x}}_{k-1}$$

- (b) Project the error covariance ahead

$$\mathbf{P}_k^- = \mathbf{A}\mathbf{P}_{k-1}\mathbf{A}^T + \mathbf{Q}$$

2. Measurement update

- (a) Compute the Kalman gain

$$\mathbf{K}_k = \mathbf{P}_k^- \mathbf{H}^T (\mathbf{H}\mathbf{P}_k^- \mathbf{H}^T + \mathbf{R})^{-1}$$

- (b) Update estimate with measurement \mathbf{z}_k

$$\hat{\mathbf{x}}_k = \hat{\mathbf{x}}_k^- + \mathbf{K}_k(\mathbf{z}_k - \mathbf{H}\hat{\mathbf{x}}_k^-)$$

- (c) Update the error covariance

$$\mathbf{P}_k = (\mathbf{I} - \mathbf{K}_k\mathbf{H})\mathbf{P}_k^-$$

To start the iteration, initial estimates for $\hat{\mathbf{x}}_{k-1}$ and \mathbf{P}_{k-1} are needed. For the case in hand, an initial state vector $\hat{\mathbf{x}}_0 = [0 \ 0 \ 0]^T$ has been chosen. Since the initial state is a guess, the starting covariance matrix \mathbf{P}_0 has been set to a large value. In fact, matrix \mathbf{P} is an indicator of the variability of the state: if \mathbf{P}_k is large, it means that the state is estimated to change a lot.

The velocity obtained applying the Kalman filter has been compared to the one obtained by integration and filtering (by means of a fourth-order Butterworth filter with cut-off frequency set at 5 Hz) of the accelerometer data. The comparison is shown in Fig.(5.10), a magnification of the signals is shown in Fig.(5.11). As

can be seen, they are virtually identical, which means both methods are valid in terms of performance. The drawback which limits the use of the Kalman filter is related to the need of measuring both acceleration and displacement, which is not something that is usually done during tests. In addition, when integrating and filtering the acceleration data, the only parameter that has to be defined is the filter cut-off frequency, which has a more intuitive meaning than the process noise covariance in the Kalman filter.

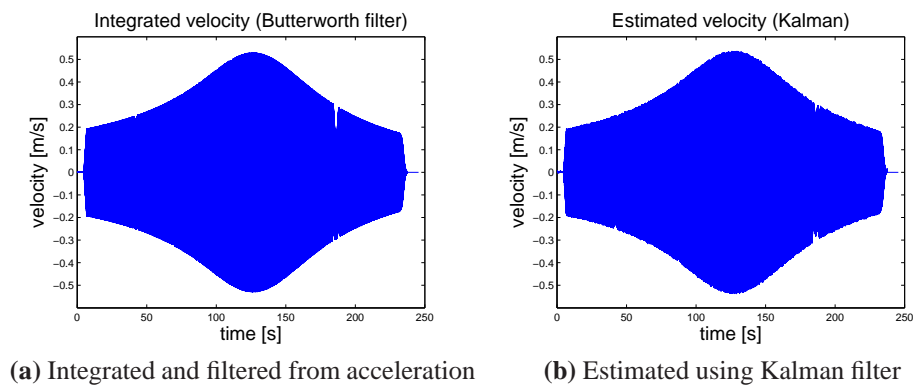


Figure 5.10: Comparison between integrated and estimated velocity

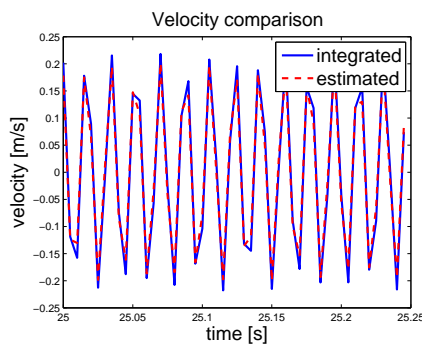


Figure 5.11: Magnification of Fig.(5.10)

Chapter 6

Application to a real-life structure: the IXV flap

Now that the method has been proved to be reliable as far as the identification of non-linear systems is concerned, it can be applied to an industrial case in which a non-linearity showed up during the testing phase. It has to be underlined that the tests conducted on this structure were not meant for this purpose and this will affect the final identification results, as will be shown.

Once the non-linearity has been identified, the parameters are used to update the FE model and a non-linear transient analysis is run to check if the improved model is capable of predicting the behaviour of the real structure.

To the author's knowledge, the application of the Restoring Force Surface method to experimental data obtained from tests on a real structure has not been attempted before. In fact, in [15] the method was applied on numerical data coming from the finite element model of a real-life structure, in which the non-linearities were modelled as non-linear springs.

The experimental data showed in this chapter and the FE model used for the numerical simulations were provided by Thales Alenia Space Italia (TAS-I).

6.1 The Intermediate eXperimental Vehicle

The Intermediate eXperimental Vehicle (IXV) is an European Space Agency (ESA) experimental re-entry vehicle, which is intended to validate re-entry technologies for future European reusable launchers [36]. The IXV project, which was successfully launched on 11 February 2015 performing a 100-minute mission, sees Thales Alenia Space Italia as the major contractor.

The main objective of the project is the design and the development, up to in-flight verification, of an autonomous European lifting and aerodynamically controlled re-entry system.

6.1.1 Mission overview

The IXV was launched on ESA's Vega rocket from Europe's Spaceport in French Guyana into a suborbital path that allows the vehicle to conduct a re-entry that resembles, as closely as possible, a Low Earth Orbit re-entry.

The IXV journey began at spacecraft separation from the Vega's upper stage: from that moment on, the IXV covered a ballistic segment that led it towards the Pacific Ocean. During this phase, IXV performed autonomously the attitude manoeuvres that allowed it to remain within a certain attitude corridor to ensure its transmitters were in a favorable position for visibility from the ground stations.

During the re-entry phase the two aerodynamic flaps were enabled and the flight control system began sending commands in the form of opening times of the thrusters valves and desired flap deflection settings, in order to reach the target condition for the trigger of the parachutes. The deployment of the parachutes allowed to slow the spacecraft down and to make it landing in the Pacific Ocean where it waited for the recovery after having deployed the flotation balloons.

The mission profile is shown in Fig.(6.1). IXV was closely monitored during the mission by the Mission Control Centre at the Advanced Logistics Technology Engineering Centre (ALTEC) in Turin, Italy.

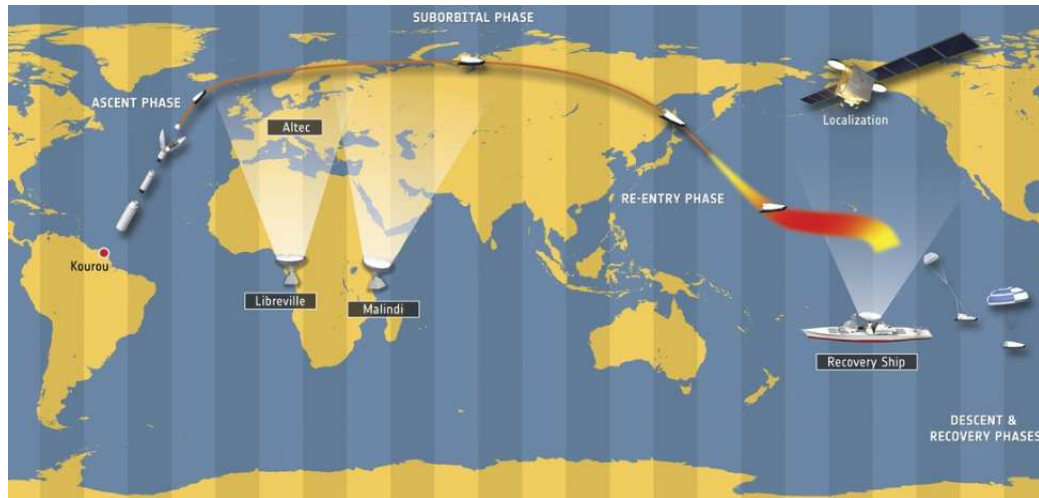


Figure 6.1: IXV mission profile (Courtesy of ESA)

6.1.2 The vehicle

The spacecraft (Fig. 6.2) is a lifting-body with no wings, with a total length of 5.0 m , width of 2.2 m and height of 1.5 m . The outer surface of the vehicle consists of advanced ceramic and ablative thermal protection materials that are able to withstand the extreme thermo-mechanical environment encountered during re-entry to protect the vehicle's structural integrity and functionality throughout the re-entry process. The inner elements are built around a carbon-fibre reinforced polymer structural panels, which provide strength and stiffness. From front to rear, the IXV spacecraft hosts a number of different systems: the avionics, the parachute and floating systems and, in the aft of the vehicle, the control actuators (the electromechanical systems to control the flaps, the propulsion module and the thrusters).

The flight control is guaranteed by reaction thrusters during the orbital phase and by two aerodynamic body flaps during the atmospheric re-entry phase. The Flap Control System (FpCS) is in charge of providing the motion and controlling the position of the two flaps during re-entry, becoming active when the efficiency of the aerodynamic control surfaces increases with the dynamic pressure.

The flaps, developed under the responsibility of Thales Alenia Space Italia, are used to provide control during re-entry, their motion being controlled by the FpCS through the elongation and retraction of two Electro-Mechanical Actuators

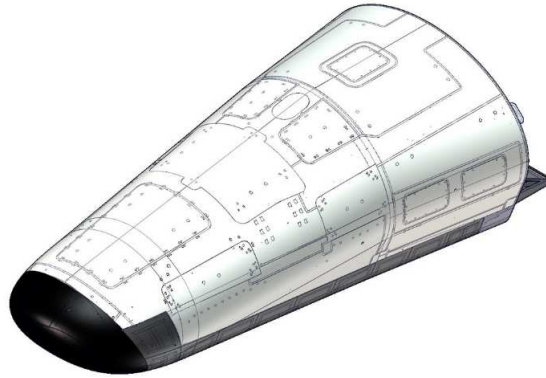


Figure 6.2: IXV external layout (Courtesy of Thales Alenia Space Italia)

(EMA), shown in Fig.(6.3). Each FpCS actuator is equipped with a locking mechanism [37], that holds the flaps in a fixed position during the launch phase, the orbital flight and the last part of the descent (with the parachutes). The IXV flaps are actuated by the FpCS during the re-entry phase and the locking mechanism holds their position when the FpCS is un-powered.



Figure 6.3: Flap Control System (Courtesy of Thales Alenia Space Italia)

6.2 Experimental results

The flap was tested on a shaking table (Fig.6.4) under a sine-sweep excitation band-limited in the frequency range $5 - 100 \text{ Hz}$, the sweep rate was set to 4 oct/min and the acceleration was enforced in the out of plane direction.

Different levels of excitation were tested and the acceleration responses were measured and stored with sampling frequency of 6.5 kHz . Since during structural tests the responses are usually stored as frequency domain data, the resulting time histories of some of them were not available.



Figure 6.4: Flap testing set-up (Courtesy of Thales Alenia Space Italia)

The input excitations of the two tests taken into consideration are the first and the second shown in Fig.(6.5).

Looking at the frequency responses obtained from the tests (Fig. 6.6), it is clear that three modes participate to the response and this will negatively affect the identification results, as will be explained later.

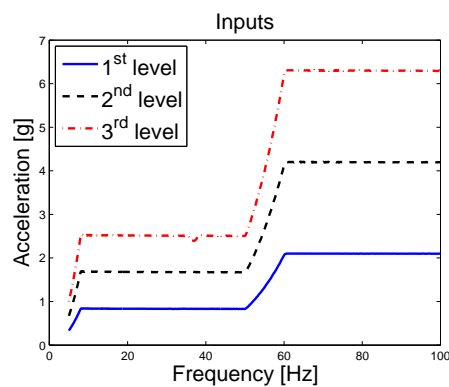


Figure 6.5: Input excitations IXV test (Courtesy of Thales Alenia Space Italia)

The presence of the non-linearity is clearly visible when comparing the transmissibilities for the different excitation levels (Fig. 6.7), in fact, the

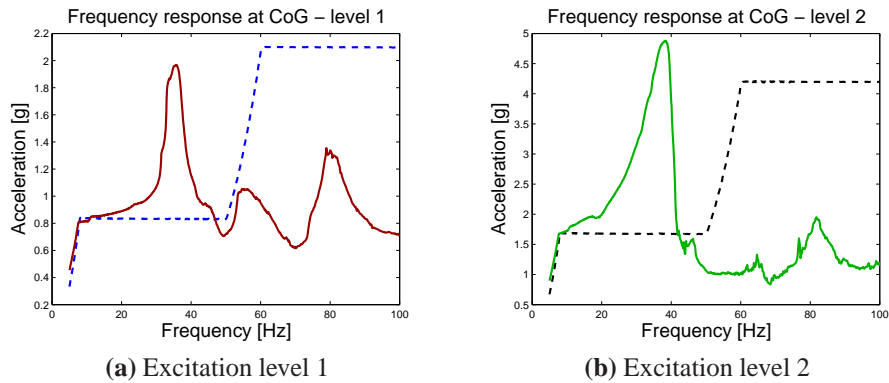


Figure 6.6: Frequency responses from test (Courtesy of Thales Alenia Space Italia)

resonance frequency shifts towards higher frequencies (from 32.63 Hz to 36.53 Hz), therefore the non-linearity is expected to be of the hardening type.

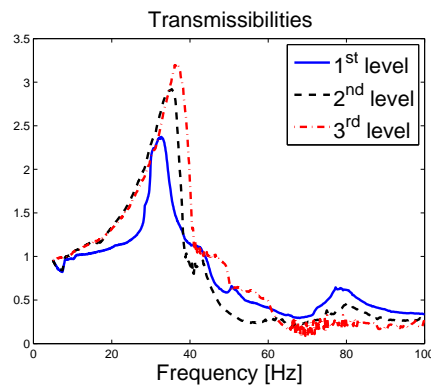


Figure 6.7: Homogeneity test - IXV flap (Courtesy of Thales Alenia Space Italia)

Being the tip the part that vibrates the most, and therefore the one that gives the highest evidence of the presence of the non-linearity, the first attempt implied the use of the acceleration measurement coming from the tip accelerometer. Unfortunately, looking at the response (Fig. 6.8) is clear that the contribution of the third mode (torsional) is far from being negligible. Moreover, the contribution of that mode could not be filtered out, otherwise all the harmonics generated by the non-linearity would have been lost. Since the Restoring Force Surface method is meant to deal with SDOF systems, this measurement had to be discarded.

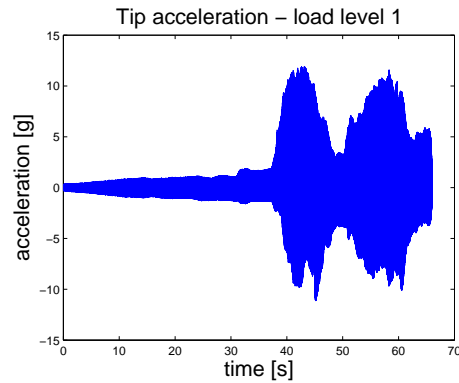


Figure 6.8: Acceleration measured at the tip (Courtesy of Thales Alenia Space Italia)

The second choice was the accelerometer placed at the centre of mass, which gave the time histories shown in Fig.(6.9). The contribution of the higher modes is still present (and can not be removed for the reason explained earlier), but it is not so significant. It has to be noted however, that the presence of other modes will negatively affect the identification results, because the structure does not behave exactly as an SDOF system.

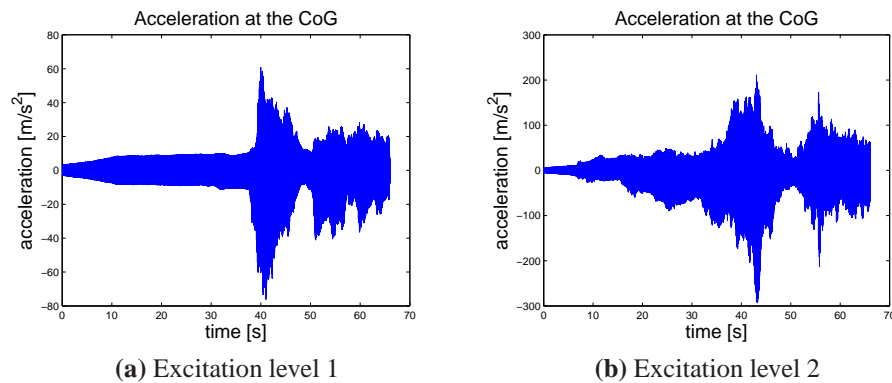


Figure 6.9: Acceleration measured at the centre of mass for both excitation levels (Courtesy of Thales Alenia Space Italia)

6.3 Non-linearity parameters identification

The excitation is given as enforced base acceleration, therefore the formulation to be used for the restoring force computation is the one explained in Section 2.1.2.

The procedure to compute the relative displacement w_L and velocity \dot{w}_L is the following: first the time history of the input acceleration (Fig. 6.10) has to be retrieved from the frequency data by means of equations (3.1),(3.4), then both the input acceleration \ddot{e}_b and the measured acceleration \ddot{y} have to be integrated and filtered as explained in Section 2.2. As last step, the input and output signals have to be synchronized to be finally able to compute the relative quantities.

To correctly scale the restoring force, the effective mass is needed and it was found to be equal to the 42.95% of the total mass.

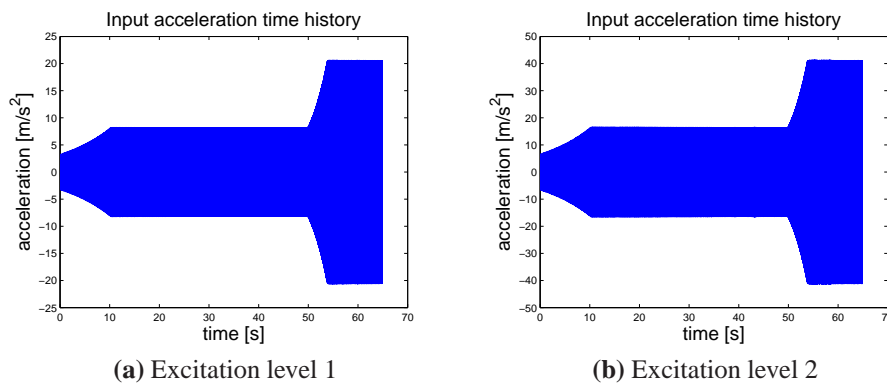


Figure 6.10: Input acceleration time histories

The Restoring Force Surface method is first applied to the data obtained from the first test. As can be seen in Fig.(6.11), the behaviour is not linear but, due to the contribution coming from the other modes, it is not possible to state without doubt that the distortions are caused by the non-linearity only. In addition, it is not possible to identify a clear non-linear trend comparable with one of the theoretical curves that represent the most common non-linearities.

By contrast, when applying the identification method to the data coming from the second test, the stiffness curve clearly shows a piecewise linear trend (Fig. 6.12b), which is typical of clearance non-linearities, though the surface shown in Fig.(6.12a) looks distorted if compared to the ones obtained from the FE model of the plate (Fig. 4.6 and 4.8).

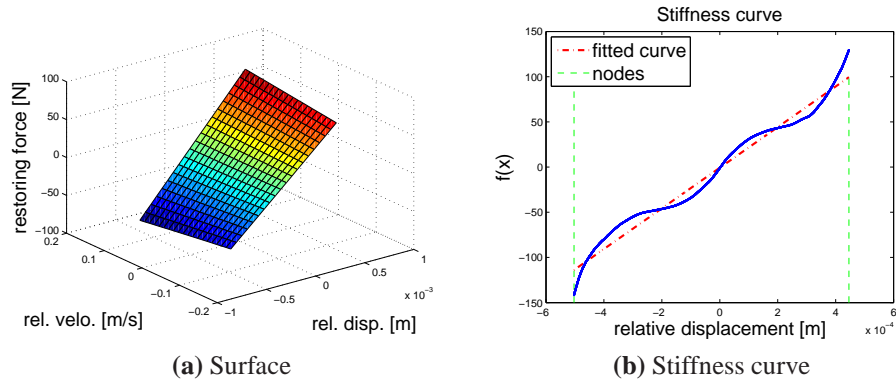


Figure 6.11: Restoring Force Surface method applied to the data from the first test

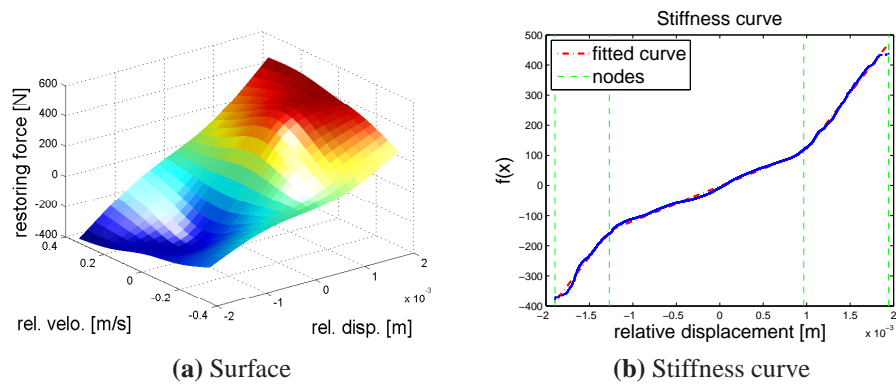


Figure 6.12: Restoring Force Surface method applied to the data from the second test

Due to the fact that it is not possible to rely on theoretical formulations to compute an estimate of the stiffness values, the identification process was focused on the determination of the gap size only. However, if the aim of the identification process is the update of the FE model, the clearance value is the only parameter needed to model the gap by means of the CGAP card. The identified clearance values are collected in Table(6.1).

d_1 [m]	d_2 [m]
-0.0013	0.0010

Table 6.1: Identified clearance values

6.4 FE model update

Once the parameters which describe the non-linearity have been identified, the FE model can be updated in order to check its capability of predicting the behaviour of the flap for different load levels.

The set-up of the analysis input files follows the guidelines highlighted in Chapter 4.

First of all, a linear transient analysis (SOL109) and a modal frequency response solution (SOL111) have been run applying the first load level used in the test. The inputs shown in Fig.(6.5a) and (6.10a) have been applied to the structure as enforced acceleration by means of the Large Mass Method. The out-of-plane responses of the node corresponding to the accelerometer position during the test are plotted in Fig.(6.13). The difference between these responses and the ones obtained from the test (Fig. 6.6a and Fig. 6.9a) is evident.

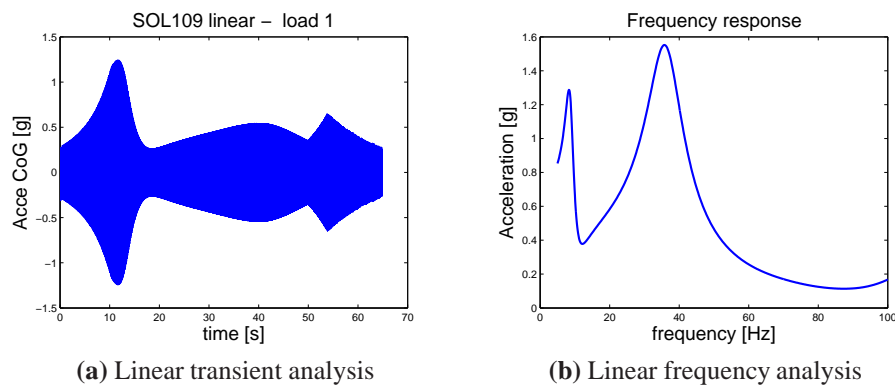


Figure 6.13: Acceleration responses at CoG for excitation level 1

6.4.1 Non-linear transient analysis

A non-linear transient analysis (SOL129) has been run without introducing any non-linearity, in such a way to check the correctness of the set-up. A look at the input excitation seen by the enforced node made clear that the input was not reproduced correctly (see Fig. 6.14 compared to Fig. 6.10a). Several simulations run to understand the reason of this behaviour showed that the problem was likely to be due to the accumulation of numerical errors, therefore the simulation was

shortened. In Fig.(6.15) the applied input and the acceleration response at the centre of mass are shown.

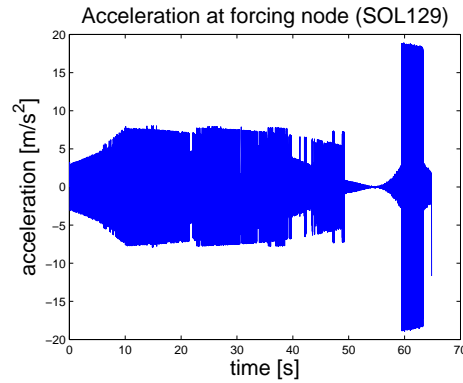


Figure 6.14: Acceleration at the enforced node

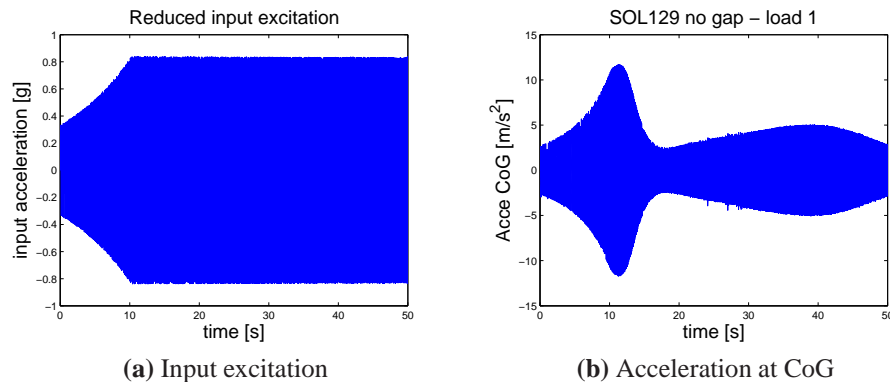


Figure 6.15: Input excitation and acceleration response obtained running a linear SOL129 (without the gap element)

Once the analysis set-up has been verified, the actual gap can be modelled thanks to the parameters identified by means of the Restoring Force Surface method applied previously (see Section 6.3). The location of the gap was identified to be at the hinge bearing, where it was meant to accommodate the distortions caused by thermal and pressure effects. Therefore, the gap has been modelled at one hinge bearing (Fig. 6.16) and in one direction only since only one set of measurements (the out of plane ones) have been taken into account during the non-linearity identification phase.

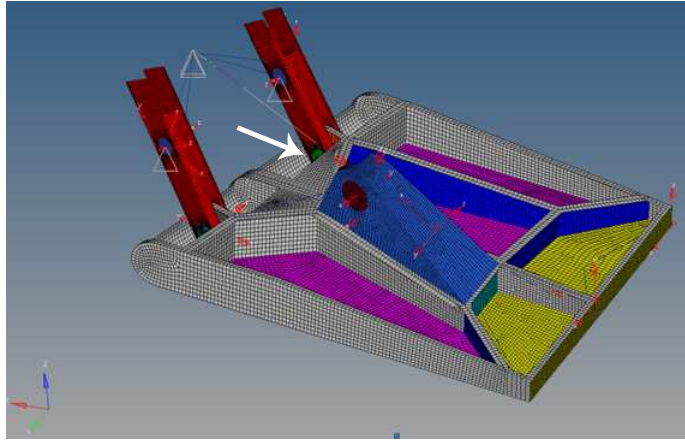


Figure 6.16: Flap FE model (Courtesy of Thales Alenia Space Italia)

The non-linear transient analysis has been run for both excitation levels and yields the results shown in Fig.(6.18). These responses seem to match the trend of the ones obtained from the test (Fig. 6.9), but for the spike in the first few seconds of simulation, which is probably due to instabilities in the numerical solution caused by the damping definition. In fact, being the SOL129 a direct transient solution, the damping had to be defined by means of the `PARAM,G` and the `PARAM,W3` parameters. This means that the damping is correct only for the frequency selected by the `PARAM,W3`¹. The effects of the different choices of the `PARAM,W3` can be seen comparing Fig.(6.13a) to Fig.(6.17), where the `W3` parameter has been set to 50.26 rad/s in the first figure and to 194.78 rad/s in the second (the frequencies selected to compute the parameter are the resonance frequencies of the structure with and without the gap). From the comparison it is evident that in Fig.(6.17) the lower frequencies are enhanced, whereas in Fig.(6.13a) the higher frequencies are more damped. The spikes visible in Fig.(6.18) come from the contribution of the low frequency mode also visible in Fig.(6.17).

Nevertheless, the resonance is reached at the same time instant of the test and the *jump phenomenon* becomes more evident as the excitation level increases. However, the amplitude of the peak is not reproduced correctly, probably

¹Every frequency lower than that one sees a lower damping and every frequency greater than `W3` gets more damping

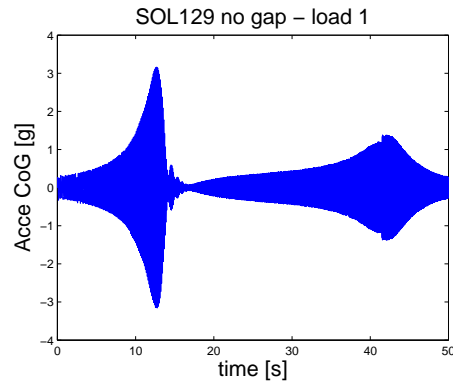


Figure 6.17: Time response obtained for $W3 = 194.78 \text{ rad/s}$

because the non-linearity present in the real system is more complex than the one that has been modelled. Looking at the frequency responses obtained by applying the Fourier transform to the time histories obtained from the Nastran simulations, the effect of the non-linearity becomes even more visible and the hardening behaviour is reproduced correctly (the resonance frequency shifts towards higher frequencies). However, the responses show a lower amplitude if compared to the ones measured during the test (Fig.6.6). An improvement in the non-linear behaviour could be obtained modelling the gap in more than one direction to try to better simulate the hinge behaviour.

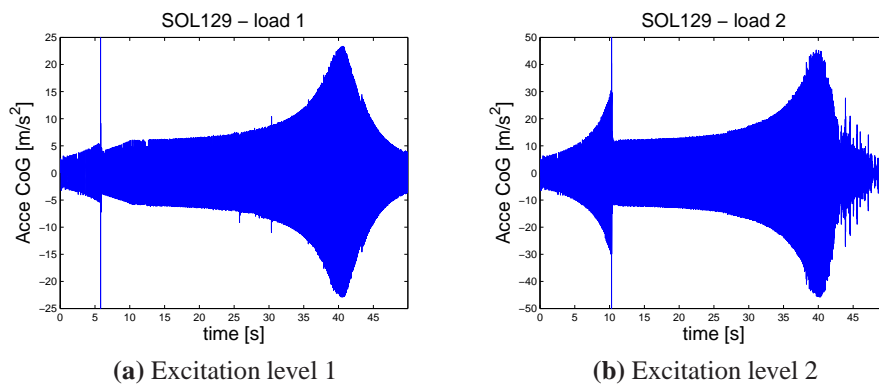


Figure 6.18: Acceleration responses at CoG in the presence of the gap

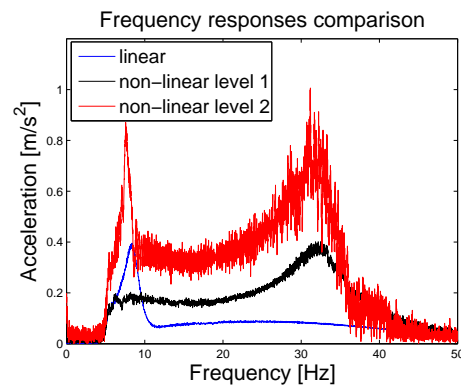


Figure 6.19: Frequency responses calculated from transient responses

Chapter 7

Conclusions and Future Work

The study aimed at applying the Restoring Force Surface method to a real-life structure, the IXV flap, in such a way to characterize the non-linearity which showed up during the testing phase. Once the non-linear parameters were identified, they were used to update the Finite Element Model of the flap in order to make it capable of reproducing the flap behaviour for different load levels.

Before reaching this final step, the method implementation has been verified by means of several numerical examples representative of different types of non-linearities, showing that the technique can be applied to a wide range of non-linearity types.

As an intermediate step between the numerical examples and the real case, a simple experiment has been prepared in order to test the method on experimental data obtained under controlled conditions.

The studied cases confirm that the Restoring Force Surface method is an efficient tool as far as the identification of SDOF systems is concerned and that it is capable of providing powerful insight into the dynamics of these systems. However, since it requires the knowledge of acceleration, velocity and displacement signals, great effort has to be spent in processing the data.

Since the study focused on stiffness non-linearities mainly, future work is needed to take into account the damping contribution.

For what concerns the Finite Element modelling of the non-linearities, the study focused on two different ways of modelling the clearance non-linearity.

The first one relied on the use of the CGAP and PGAP cards, which define a gap element, whereas the second one implied the use of non-linear load functions (NOLINI cards) to generate direct forces from displacement functions. Both strategies have been successfully applied both in time and frequency domains on the simple case of the plate whereas in the case of the IXV flap the non-linearity has been modelled by means of the gap element in a non-linear transient analysis only. A possible direction for future studies could be the modelling of the non-linearity in the frequency domain so that the numerical results could be directly compared to the test results, usually presented in the form of frequency responses and/or transmissibility functions.

For what concerns the FE model of the flap, future work should take into account the possibility of modelling the gap in more than one direction by means of the NLRGAP card, which allows to define a non-linear radial gap and works for both transient and frequency solutions. Another step towards a more realistic model of the hinge behaviour could be the inclusion of the dry friction effects.

Appendix A

Harmonic Balance Method

The Harmonic Balance Method [4] [5] allows for analysing the steady-state fundamental harmonic non-linear structural response due to harmonic excitation in the frequency domain (a generalisation of the method to inputs other than a sinusoid can be found in [35] and it has been applied in [17]). The transformation to the frequency domain is done by calculating equivalent stiffness and damping parameters for the non-linear elements which would prevent such transformation.

For a SDOF system, the non-linear equation of motion can be written as

$$m\ddot{y}(t) + f_R(y, \dot{y}) = p(t) \quad (\text{A.1})$$

where $f_R(y, \dot{y})$ is a non-linear restoring force function.

The fundamental assumption behind the Harmonic Balance Method is that the response of a non-linear system due to harmonic excitation can be approximated by a harmonic function in the frequency of excitation, i.e. the total non-linear response of the system is dominated by the fundamental harmonic response:

$$p(t) = P \sin(\Omega t + \phi) \rightarrow \begin{cases} y(t) \approx Y \sin(\Omega t) \\ \dot{y}(t) \approx \Omega Y \cos(\Omega t) \\ \ddot{y}(t) \approx -\Omega^2 Y \sin(\Omega t) \end{cases} \quad (\text{A.2})$$

If this assumption is fulfilled, the non-linear restoring force function $f_R(y, \dot{y})$

can be decomposed into a Fourier series truncated after the fundamental terms

$$f_R(y, \dot{y}) = a_0 + a_1 \sin(\Omega t) + b_1 \cos(\Omega t) \quad (\text{A.3})$$

where a_0 , a_1 and b_1 are the Fourier coefficients which can be calculated from the following integrals

$$a_0 = \frac{1}{2\pi} \int_0^{2\pi} f_R(y, \dot{y}) d(\Omega t) \quad (\text{A.4a})$$

$$a_1 = \frac{1}{\pi} \int_0^{2\pi} f_R(y, \dot{y}) \cos(\Omega t) d(\Omega t) \quad (\text{A.4b})$$

$$b_1 = \frac{1}{\pi} \int_0^{2\pi} f_R(y, \dot{y}) \sin(\Omega t) d(\Omega t) \quad (\text{A.4c})$$

The aim of applying the Harmonic Balance Method is approximating the non-linear restoring force function by equivalent spring and damper forces

$$f_R(y, \dot{y}) = k_{eq} Y \sin(\Omega t) + c_{eq} \Omega Y \cos(\Omega t) \quad (\text{A.5})$$

A comparison of the coefficients of equations(A.3) and (A.5) yields the equations from which the stiffness and damping parameters can be identified

$$k_{eq}(Y) = \frac{b_1}{Y} \quad (\text{A.6a})$$

$$c_{eq}(Y) = \frac{a_1}{\Omega Y} \quad (\text{A.6b})$$

The equivalent parameters in equation(A.6) are dependent on the amplitude Y of the harmonic displacement response. Since Y is unknown at the beginning of the response analysis, the determination of the equivalent parameters has to be performed iteratively.

The bilinear spring case

The result presented in Chapter 3 about the equivalent non-linear stiffness in the case of a bilinear spring is here explained in details.

As already said, the bilinear stiffness has the following form

$$f_s(y) = \begin{cases} k_1 y & y < y_c, \\ k_2 y + (k_1 - k_2)y_c & y \geq y_c \end{cases} \quad (\text{A.7})$$

The equivalent stiffness is given by equation(A.6a). The integrand changes when the displacement exceeds y_c and this corresponds to a point in the cycle $\theta_c = \Omega t_c$ where

$$\theta_c = \sin^{-1}\left(\frac{y_c}{Y}\right) \quad (\text{A.8})$$

Therefore the form of the bilinear stiffness becomes

$$f_s(y) = \begin{cases} k_1 y & -\pi/2 \leq \theta < \theta_c, \\ k_2 y + (k_1 - k_2)y_c & \theta_c \leq \theta \leq \pi/2 \end{cases} \quad (\text{A.9})$$

For memoryless¹, static non-linearities equation(A.6a) becomes

$$k_{eq} = \frac{2}{\pi Y} \int_{-\pi/2}^{\pi/2} f_s(y) \sin \theta d\theta \quad (\text{A.10})$$

where $y = Y \sin \theta$. Substituting equation(A.9) into equation(A.10)

¹static, single-valued characteristics are termed memoryless, i.e. the output is uniquely defined by the input value: $y(t) = F(x(t))$, where $y = F(x)$ is an injective function (each x is mapped to only one value y)

$$\begin{aligned}
k_{eq} &= \frac{2}{\pi Y} \int_{-\pi/2}^{\theta_c} k_1 Y \sin^2(\theta) d\theta + \frac{2}{\pi Y} \int_{\theta_c}^{\pi/2} \left[k_2 Y \sin \theta + (k_1 - k_2) y_c \right] \sin \theta d\theta \\
&= \frac{2k_1}{\pi} \int_{-\pi/2}^{\theta_c} \frac{1 - \cos(2\theta)}{2} d\theta + \frac{2y_c}{\pi Y} (k_1 - k_2) \int_{\theta_c}^{\pi/2} \sin \theta d\theta + \frac{2k_2}{\pi} \int_{\theta_c}^{\pi/2} \frac{1 - \cos(2\theta)}{2} d\theta \\
&= \frac{2k_1}{\pi} \left[\frac{\theta_c}{2} + \frac{\pi}{4} - \frac{\sin(2\theta_c)}{4} \right] + \frac{2y_c}{\pi Y} (k_1 - k_2) \cos \theta_c + \frac{2k_2}{\pi} \left[\frac{\pi}{4} - \frac{\theta_c}{2} + \frac{\sin(2\theta_c)}{4} \right]
\end{aligned}$$

After some algebra

$$k_{eq} = k_1 + \frac{k_2 - k_1}{2\pi} \left(\pi - 2\theta_c + \sin(2\theta_c) - \frac{4y_c}{Y} \cos(\theta_c) \right) \quad (\text{A.11})$$

If $y_c = 0$, then also $\theta_c = 0$ because of equation(A.8). Therefore equation(A.11) yields the result presented in Chapter 3

$$k_{eq} = k_1 + \frac{k_2 - k_1}{2} = \frac{1}{2}(k_1 + k_2) \quad (\text{A.12})$$

Clearance non-linearity

The clearance non-linearity is described by equation(A.13)

$$f_s(y) = \begin{cases} k_2(y - y_c) & y > y_c \\ 0 & |y| \leq y_c \\ k_2(y + y_c) & y < -y_c \end{cases} \quad (\text{A.13})$$

Again, the integrand changes when the displacement exceeds y_c and this corresponds to a point in the cycle $\theta_c = \Omega t_c$ where θ_c is given by equation(A.8), thus yielding

$$f_s(y) = \begin{cases} 0 & 0 < \theta \leq \theta_c \\ k_2(y - y_c) & \theta_c < \theta < \pi/2 \end{cases} \quad (\text{A.14})$$

The equivalent stiffness can be computed by solving equation(A.15), which holds for odd, memoryless, static non-linearities:

$$k_{eq} = \frac{4}{\pi Y} \int_0^{\pi/2} f_s(y) \sin \theta d\theta \quad (\text{A.15})$$

Substituting the expression of $f_s(y)$ yields

$$\begin{aligned} k_{eq} &= \frac{4}{\pi Y} \int_{\theta_c}^{\pi/2} k_2(Y \sin \theta - y_c) \sin \theta d\theta \\ &= \frac{4k_2}{\pi} \int_{\theta_c}^{\pi/2} \sin^2 \theta d\theta - \frac{4k_2 y_c}{\pi Y} \int_{\theta_c}^{\pi/2} \sin \theta d\theta \\ &= \frac{4k_2}{\pi} \int_{\theta_c}^{\pi/2} \frac{1 - \cos(2\theta)}{2} d\theta - \frac{4k_2 y_c}{\pi Y} \cos \theta_c \\ &= \frac{k_2}{\pi} \left[\pi - 2\theta_c + \sin(2\theta_c) - \frac{4y_c}{Y} \cos \theta_c \right] \end{aligned}$$

Substituting equation(A.8) and knowing that $\cos[\sin^{-1}(x)] = \sqrt{1 - x^2}$, the previous expression simplifies as follows

$$\begin{aligned} k_{eq} &= \frac{k_2}{\pi} \left[\pi - 2 \sin^{-1} \left(\frac{y_c}{Y} \right) + 2 \sin \theta_c \cos \theta_c - \frac{4y_c}{Y} \sqrt{1 - \left(\frac{y_c}{Y} \right)^2} \right] \\ &= \frac{k_2}{\pi} \left[\pi - 2 \sin^{-1} \left(\frac{y_c}{Y} \right) - \frac{2y_c}{Y} \sqrt{1 - \left(\frac{y_c}{Y} \right)^2} \right] \end{aligned} \quad (\text{A.16})$$

Appendix B

Nastran input files

Linear solution sequences

SOL108	Direct frequency response
SOL109	Direct transient response
SOL111	Modal frequency response
SOL112	Modal transient response

Non-linear solution sequences

SOL128	Non-linear harmonic response
SOL129	Non-linear transient response
SOL400	Implicit non-linear transient response

Listing B.1: Modal Frequency Response (SOL111) - Linear plate

```

$ Frequency Analysis
SOL 111
CEND
TITLE = *PLATE*
ECHO = NONE
$
SDAMPING = 1
SUBCASE 1
$ Subcase name : modal_frequency
  METHOD = 1
  DLOAD = 2
  SPC = 2
  FREQUENCY = 66
  SPCFORCES(SORT1,REAL) = ALL
  OLOAD = ALL
OUTPUT (XYPLOT)
PLOTTER NAST
XYPUNCH ACCE /176(T3)
XYPUNCH VELO /176(T3)
XYPUNCH DISP /176(T3)
XYPUNCH OLOAD /32(T3)
$
BEGIN BULK
$
PARAM      POST      0
PARAM      PRTMAXIM YES
$
$FREQ1     SID       F1       DF       NDF
FREQ1     66        10.      .5      980
$
TABDMP1    1         CRIT
           20.      .03     300.    .03     ENDT
$
EIGRL     1         -0.1    3000.   0
$
$ Elements and Element Properties for region : shell_mat
PSHELL    1         1         .0012   1         1
$ Pset: "shell_mat" will be imported as: "pshell.1"
CQUAD4    1         1         1         2         34         33
$.
$.
$.
CQUAD4    341      1         351      352      384      383
$
$ Material :
MAT1*     1         7.0E+10      .3
*         2770.
$ Nodes of the Entire Model
GRID      1         0.         0.         0.
$.
$.
$.
GRID*     384         .127000004053116.050799999386072
*         0.
$
$ Constraints
$
SPCADD    2         1         996
$
SPC1      1         123456  1         353

```

```

$
SPC      996      167      123
$
$ Dynamic loading
$
$DLOAD  SID  S      S1      L1
DLOAD   2    1.    1.      88
$
$RLOAD2 SID  EXCID  DELAY  DPHASE  TB      TP      TYPE
RLOAD2  88  99      300.    90      89      0
$
$DAREA  SID  P1      C1      A1
DAREA   99  32      3      1.
$
TABLED1 89
        10.    1.    500.    1.    ENDT
$
ENDDATA

```

Listing B.2: Modal Transient Response (SOL112) - Linear plate

```

$ Transient Analysis
SOL 112
CEND
TITLE = *PLATE*
ECHO = NONE
$
SDAMPING = 1
SUBCASE 1
$ Subcase name : modal_transient
  METHOD = 1
  TSTEP = 1
  DLOAD = 2
  SPC = 2
  SPCFORCES(SORT1,REAL) = ALL
  OLOAD = ALL
OUTPUT (XYPLOT)
PLOTTER NAST
XYPUNCH ACCE /176(T3)
XYPUNCH VELO /176(T3)
XYPUNCH DISP /176(T3)
XYPUNCH OLOAD /32(T3)
$
BEGIN BULK
$
PARAM   POST    0
PARAM   PRTMAXIM YES
$
TSTEP   1        1000    1.0-3
$
TABDMP1 1        CRIT
        20.      .03     300.    .03     ENDT
$
EIGRL   1        -0.1    3000.    0
$
$ Elements and Element Properties for region : shell_mat
PSHELL  1        1        .0012    1        1
$ Pset: "shell_mat" will be imported as: "pshell.1"
CQUAD4  1        1        1        2        34        33
$.
$.

```

```

$.
CQUAD4  341    1    351    352    384    383
$
$ Material :
MAT1*   1          7.0E+10          .3
*
* 2770.
$ Nodes of the Entire Model
GRID    1          0.    0.    0.
$.
$.
$.
GRID*   384          .127000004053116.0507999999386072
*
* 0.
$
$ Constraints
$
SPCADD  2    1    996
$
SPC1    1    123456  1    353
$
SPC     996    167    123
$
$ Dynamic loading
$
$DLOAD  SID  S    S1    L1
DLOAD   2    1.    1.    88
$
$TLOAD2 SID  EXCID  DELAY  TYPE  T1    T2    F    P
TLOAD2  88    99          0    0.0    1.    79.26  -90.
$
$DAREA  SID  P1    C1    A1
DAREA   99    32    3    1.
$
ENDDATA

```

Appendix C

Macaulay's method for beam deflection

Considering the cantilever beam shown in Fig.(C.1), the deflection at any point can be determined applying the Macaulay's method, which allows to represent the bending moment $M(x)$ by a single analytical function even in case of concentrated loads like the one showed in the figure.

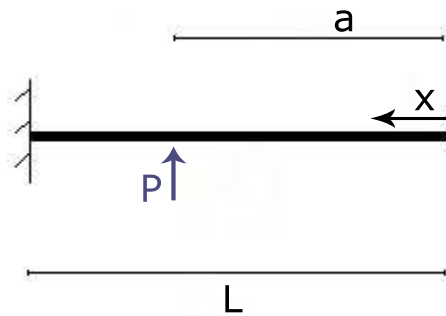


Figure C.1: Scheme of cantilever beam to apply the Macaulay's method

To determine the equation of the elastic curve for the beam in Fig.(C.1), it is necessary to consider two portions and determine the function $y(x)$ which defines the elastic curve for each of these portions.

$$EI \frac{d^2y}{dx^2} = M(x) \quad (C.1)$$

For $0 \leq x < a$, the bending moment M_1 is zero (as can be easily seen drawing the free-body diagram). Whereas, considering the portion for $a \leq x \leq L$, the bending moment is expressed as $M_2(x) = P(x - a)$. The two functions $M_1(x)$ and $M_2(x)$ can be represented by the single expression

$$M(x) = P\langle x - a \rangle \quad (\text{C.2})$$

where the brackets $\langle \dots \rangle$ should be replaced by ordinary parentheses when $x \geq a$ and by zero when $x < a$. These brackets are termed Macaulay's brackets and they are defined as

$$\langle x - a \rangle = \begin{cases} 0 & \text{if } x < a \\ x - a & \text{if } x \geq a \end{cases}$$

and the expression has to be integrated as follows (for $n \geq 0$)

$$\int P\langle x - a \rangle^n dx = \frac{P}{n+1} \langle x - a \rangle^{n+1} + C$$

Substituting the expression of $M(x)$ into the equation of the elastic curve and assuming $P = 1$, the equation to be integrated twice is

$$EI \frac{d^2y}{dx^2} = \langle x - a \rangle \quad (\text{C.3})$$

which gives

$$\begin{aligned} EI \frac{dy}{dx} &= \frac{1}{2} \langle x - a \rangle^2 + A \\ EI y(x) &= \frac{1}{6} \langle x - a \rangle^3 + Ax + B \end{aligned}$$

The constants A and B can be determined from the boundary conditions as follows

$$\text{at } x = L \begin{cases} \frac{dy}{dx} = 0 \longrightarrow A = -\frac{1}{2}(L - a)^2 \\ y = 0 \longrightarrow B = \frac{L}{2}(L - a)^2 - \frac{1}{6}(L - a)^3 \end{cases}$$

The expression for the beam deflection is therefore

$$y(x) = \frac{1}{6EI} [x - a]^3 - 3(L - a)^2 x + 3(L - a)^2 L - (L - a)^3 \quad (\text{C.5})$$

Appendix D

Kalman filter MATLAB code

Listing D.1: MATLAB function for discrete Kalman filter

```
1 function [x,P] = kalman_filter(x,z,A,P,H,R,Q)
2
3 % System's governing equations:
4 %
5 %  $x = Ax + Bu + q$ 
6 %  $z = Hx + r$ 
7 %
8 % Vector Variables
9 %
10 % x : state vector (n,1)
11 % z : observation vector (m,1) where  $m < n$ 
12 %
13 % Matrix Variables
14 %
15 % A : state transition matrix (n,n)
16 % H : observation matrix (m,n)
17 % P : covariance of the state vector (x) estimate (n,n)
18 % Q : process noise covariance (n,n)
19 % R : measurement noise covariance (m,m)
20 %
21 % Variables omitted from this model
22 %
23 % u : input control vector
24 % B : input matrix
25
26 % Positive-semidefinite check for R and Q matrices
27 [~,pq] = chol(Q);
28 [~,pr] = chol(R);
29
30 if pq > 0
31     error('Matrix Q is not positive-semidefinite')
32 end
```

```
33
34 if pr > 0
35     error('Matrix R is not positive-semidefinite')
36 end
37
38 % KALMAN FILTER
39
40 % Time update ("prediction") =====
41 % Project the state ahead
42 x = A*x;
43 % Project the error covariance ahead
44 P = A*P*A.'+Q;
45
46 % Measurement Update ("correct") =====
47 % Compute the Kalman gain
48 PH = P*H.';
49 D = H*P*H.'+R;
50 K = PH/D;
51 % Update estimate with measurement
52 x = x+K*(z-H*x);
53 % Update the error covariance
54 [n,m]= size(P);
55 P = (eye(n,m)-K*H)*P;
56
57 end
```

Abbreviations

ALTEC	Advanced Logistics Technology Engineering Centre
BDF	Backward Differentiation Formulas
CoG	Centre of Gravity
DEM	Direct Enforced Motion
EMA	Electro-Mechanical Actuators
ESA	European Space Agency
FEM	Finite Element Method
FpCS	Flap Control System
FRF	Frequency Response Function
FT	Fourier Transform
IIR	Infinite Impulse Response
IXV	Intermediate eXperimental Vehicle
LMM	Large Mass Method
MDOF	Multi Degree Of Freedom
NDF	Numerical Differentiation Formulas
ODE	Ordinary Differential Equation
RFS	Restoring Force Surface
SDOF	Single Degree Of Freedom
STFT	Short Time Fourier Transform
TAS-I	Thales Alenia Space Italia

Bibliography

- [1] G. Kerschen, K. Worden, A.F. Vakakis, J.C. Golinval, *Past, present and future of nonlinear system identification in structural dynamics*, Mechanical Systems and Signal Processing 20, 2006, pp.505-592
- [2] K. Vanhoenacker, J. Schoukens, J. Swevers, D. Vaes, *Summary and comparing overview of techniques for the detection of non-linear distortions*, Proceedings of ISMA, Volume 3, 2002
- [3] D. Göge, M. Sinapsius, U. Füllekrug, M. Link, *Detection and description of non-linear phenomena in experimental modal analysis via linearity plots*, International Journal of Non-linear Mechanics 40, 2005, pp.27-48
- [4] K. Worden, G.R. Tomlinson, *Nonlinearity in structural dynamics: detection, identification and modelling*, Institute of Physics Publishing, 2001
- [5] M. Böswald, M. Link, *Identification of non-linear joint parameters by using Frequency Response Residuals*, Proceedings of ISMA, 2004, Leuven
- [6] M. Link, M. Boeswald, S. Laborde, M. Weiland, A. Calvi, *Non-linear experimental modal analysis and application to satellite vibration test data*, COMPDYN, 2011
- [7] E.F. Crawley, K.J. O'Donnel, *Identification of non-linear system parameters in joints using the Force-State Mapping Technique*, MIT SSL Report, 1985
- [8] S. Duym, *An alternative force state map for shock absorbers*, Proceedings of the Institution of Mechanical Engineers Part D, Journal of Automobile Engineering, 1997
- [9] S. Duym, J. Schoukens, *Design of excitation signals for the Restoring Force Surface Method*, Mechanical Systems and Signal Processing, 1995, pp.139-158

- [10] S. Duym, J. Schoukens, P. Guillaume, *A local Restoring Force Surface Method*, 13th International Conference on Modal Analysis, Nashville, Tennessee, 1995, pp.1392-1399
- [11] H. Jalali, H. Ahmadian, J.E. Mottershead, *Identification of nonlinear bolted lap-joint parameters by force-state mapping*, International Journal of Solids and Structures 44, 2007, pp.8087-8105
- [12] K.Shin, J.K. Hammond, *Pseudo Force-State Mapping Method: incorporation of the embedding and Force-State Mapping Methods*, Journal of Sound and Vibration 211, 1998, pp.918-992
- [13] M.S. Allen, H. Sumali & D.S. Epp, *Restoring force surface analysis of nonlinear vibration data from micro-cantilever beams*, Proceedings of IMECE 2006, Chicago, Illinois
- [14] G. Kerschen, J.C. Golinval, K. Worden, *Theoretical and experimental identification of a non-linear beam*, Journal of Sound and Vibration 244, 2001, pp.597-613
- [15] J.P. Noel, G. Kerschen, A. Newerla, *Application of the Restoring Force Surface Method to a Real-life Spacecraft Structure*, Topics in Nonlinear dynamics, Volume 3, Proceedings of the 30th IMAC, A Conference on Structural Dynamics, 2012
- [16] G. Kerschen, L. Soula, J.B. Vergniaud, A. Newerla, *Assessment of Nonlinear System Identification Methods using the SmallSat Spacecraft Structure*, Advanced Aerospace Applications, Volume 1, Proceedings of the 29th IMAC, A Conference on Structural Dynamics, 2011
- [17] M. Manetti, G. Quaranta, P. Mantegazza, *Numerical evaluation of limit cycles of aeroelastic systems*, Journal of Aircraft, Volume 46 No.5, 2009
- [18] J.G.T. Ribeiro, J.L.F. Freire, J.T.P. de Castro, *Some comments on digital integration to measure displacements using accelerometers*, Shock and Vibration Digest, Volume 32, 2000, p.52
- [19] J.G.T. Ribeiro, J.L.F. Freire, J.T.P. de Castro, *New improvements in the digital double integration filtering method to measure displacements using accelerometers*, Proceedings of the International Modal Analysis Conference - IMAC, Volume 1, 2001, pp.538-542
- [20] Steven W. Smith, *The Scientist and Engineer's Guide to Digital Signal Processing*, Second edition, California Technical Publishing

- [21] A.V. Oppenheim, R.W. Schaffer, *Discrete-time signal processing*, Second edition, Prentice Hall
- [22] *MATLAB Product Documentation*, Release 2014b, The Mathworks Inc.
- [23] R.G. Lyons, *Understanding digital signal processing*, Second edition, Prentice Hall
- [24] G. Gloth, M. Sinapius, *Detection of Non-Linearities in Swept-Sine Measurements*, XXI International Modal Analysis Conference - IMAC, Orlando, Florida, 2003
- [25] J.A. Lollock, *The effect of swept sinusoidal excitation on the response of a single degree of freedom oscillator*, 43rd AIAA Structures, Structural Dynamics and Materials Conference, Denver, Colorado, 2002
- [26] P. Nali, A. Bettacchioli, *Beating phenomena in spacecraft sine tests and an attempt to include the sine sweep rate effect in the test-prediction*
- [27] B. Boashash, *Estimating and interpreting the instantaneous frequency of a signal - Part 1: fundamentals*, Proceedings of the IEEE, Volume 80, 1992
- [28] C. Moler, *Numerical computing with MATLAB*, Electronic Edition, MathWorks, 2004
- [29] T.D. Gilliam, *Numerical modelling of the dynamic response of a multi-bilinear spring support system*, University of Kentucky Master's Theses, 2010
- [30] MSC Nastran 2013.1, *Quick Reference Guide*
- [31] MSC Nastran 2013, *Dynamic Analysis User's Guide*
- [32] R.D. Blevins, *Formulas for Natural Frequency and Mode Shape*, Krieger, 1979
- [33] R.E. Kalman, *A new approach to linear filtering and prediction problems*, Transaction of the ASME - Journal of Basic Engineering, Volume 82, 1960, pp.35-45
- [34] G. Welch, G. Bishop, *An introduction to the Kalman filter*, 2006
- [35] A. Gelb, W.E. Vander Velde, *Multiple-input describing functions and nonlinear system design*, McGraw-Hill Book Company

- [36] E. Zaccagnino, G. Malucchi, V. Marco, A. Drocco, S. Dussy and J.P. Préaud, *Intermediate eXperimental Vechicle (IXV), the ESA re-entry demonstrator*, AIAA Guidance, Navigation and Control Conference, Portland, Oregon, 2011
- [37] D. Verhoeven, D. Renté, *Locking mechanism for the IXV re-entry demonstrator flap control system*, 14th European Space Mechanisms and Tribology Symposium - ASMATS 2011, Constance, Germany, 2011